

Investigating Deformation Styles of
Salt Detachments Using Seismic
Attribute Analysis: An Example from
the Gulf of Mexico

Thesis submitted in accordance with the requirements of the University of
Adelaide for an Honours Degree in Geology.

Nicholas Walter Eckert
November 2014



THE UNIVERSITY
of ADELAIDE

INVESTIGATING DEFORMATION STYLES OF SALT DETACHMENTS USING SEISMIC ATTRIBUTE ANALYSIS: AN EXAMPLE FROM THE GULF OF MEXICO

DEFORMATION OF THE SALT DETACHMENT IN THE GULF OF MEXICO

ABSTRACT

The current deformation style of active salt detachments beneath delta and deep-water fold-thrust belts in the Gulf of Mexico is poorly constrained. The combination of seismic interpretation and seismic attribute analysis provides greater resolution for identifying fault patterns that are otherwise unresolved in conventional seismic amplitude displays. These techniques are applied to the Ship Shoal and North-West Gulf Coast 3D seismic volumes, and used to investigate the geometry of low signal amplitudes within six interpreted salt diapirs. The ridge enhancement filter and similarity attributes display a strong correlation with faults and fractures observed over a range of magnitudes, and identify structural relationships between salt diapirs and the surrounding sedimentary overburden. Conventional seismic amplitude displays show salt diapirs as ductile and homogenous structures. However, this study concludes that diapirs are likely to contain interbedded resistive sequences facilitating brittle shear. Deformation styles exhibited by active salt diapirs are broadly comparable to those observed in outcrops within exhumed detachment systems. Future application of seismic attribute analysis is needed to improve the understanding of deformation styles exhibited by similar submarine structures.

KEYWORDS

Salt tectonics, Gulf of Mexico, salt detachment, seismic attributes analysis, salt diapirs

TABLE OF CONTENTS

Abstract.....	i
Keywords.....	i
List of Figures and Tables	iii
1. Introduction	1
2. Background	2
3. Methods.....	11
4. Salt Diapirs Identified in the Gulf of Mexico	21
5. Seismic Attribute Analysis.....	25
6. Discussion	30
7. Conclusions	39
Acknowledgments	41
References	42
Appendix A: Methodology.....	47

LIST OF FIGURES AND TABLES

Figure 1: a) Location map of the northern Gulf of Mexico basin illustrating the locations of the Ship Shoal and North-West Gulf Coast 3D seismic volumes (modified from Hudec et al. 2013a). b) Generalised cross-section of the northern Gulf of Mexico basin displaying stratigraphy and structural elements. Stratigraphy within the northern Gulf consists of a succession of Jurassic through Holocene strata (modified from Galloway 2008). 3

Figure 2: Schematic model of a delta and deep-water fold-thrust belt demonstrating a 90° rotation of maximum horizontal stress (σ_H) from margin parallel to margin normal, respectively (King et al. 2009). Normal listric growth faults form due to extension at the delta-top. Thin-skinned extension dominates the transitional zone accommodating salt and shale diapirism. Stacked thrust sheets with associated folds occur at the distal pinch-out of the detachment, forming the delta toe (modified from King and Backé 2010). 5

Figure 3: Schematic illustration of salt velocity profiles. a) Poiseuille flow in a single thick layer. b) Couette flow produced by overburden sliding. c) Combination of Poiseuille and Couette flow, displaying relative movement along resistive bounding layers. d) Poiseuille and Couette flow across multiple layers, where interbedded sequences form rigid planes (modified from Davison et al. 1996). 7

Figure 4: Three modes of salt diapirism and their characteristic structures. A reactive diapir displaying a fan of normal faults along its flanks with associated flexure of sediments. An active diapir below a radial network of faults. A passive diapir displaying near-vertical flank geometry and associated dragging of sediments (modified from Jackson et al. 1994). 9

Figure 5: Crossline 2190 of the Ship Shoal seismic volume illustrating the distortion of amplitude velocities imposed by salt. The top layer of salt is identified by strong reflectivity..... 12

Figure 6: Interpretation areas Crosslines 4842 from the North-West Gulf Coast and 2190 from the Ship Shoal 3D seismic volume containing time-slices and interpreted horizons. A) Interpreted horizons representing the top salt layer and an upper sedimentary horizon, along with time-slices taken at 2732 and 3824 ms (North-West Gulf Coast seismic volume). B) Interpreted horizons representing the top salt layer and an upper sedimentary horizon, along with time-slices taken at 2172 and 2800 ms (Ship Shoal seismic volume). 14

Figure 7: Different seismic attributes displayed on a horizontal time-slice at 1940 ms across the Ship Shoal 3D seismic volume in the Gulf of Mexico. a) Oblique view of time-slice 1940 intersecting crossline 2190 with interpreted structural features. b) Time-slice at 1940 ms of dip-steered median filtered seismic, removing random noise and enhancing laterally continuous seismic events by filtering along the structural dip. c) Dip- azimuth, computing the plane of best fit between neighbouring points and outputting the minimum (red) and maximum (blue) slope. d) Polar-dip, computing the plane or line of best fit between neighbouring points and outputs the minimum (red) and maximum (blue) magnitude of dip. e) Dip-steered minimum curvature, describing how bent a surface is at a particular point, measures the curve perpendicular to the maximum curvature and outputs its value (yellow). f) Dip-steered maximum curvature, measuring the maximum amount of bending orthogonal to the minimum curvature and outputs its value (yellow). g) Full-steered detailed similarity, a gently filtered attribute calculating

and outputting the best likeness (black), and least likeness (white), between adjacent traces by following the dips and local azimuths of the time-slice in all directions at every trace position. h) Full-steered background similarity, a heavily filtered attribute calculating and outputting the best likeness (black), and least likeness (white), between adjacent traces by following the dips and local azimuths of the time-slice in all directions at every trace position. i) Non-steered similarity, calculating and outputting the best likeness (black), and least likeness (white), between adjacent traces without dip-steering. j) Ridge enhancement filter, comparing in the time-slice domain three neighbouring similarity values in six different directions and outputs the largest ridge value (grey)..... 18

Figure 8: Different seismic attributes displayed on a horizontal time-slice at 2928 ms across the North-West Gulf Coast 3D seismic volume in the Gulf of Mexico. a) Oblique view of the intersection between time-slice 2928 and crossline 4570 with an interpreted salt diapir. b) Time-slice at 2928 ms of dip-steered median filtered amplitudes, removing random noise and enhancing lateral continuous seismic events by filtering along the structural dip. c) Dip- azimuth, computing the plane of best fit between neighbouring points and outputting the minimum (red) and maximum (blue) slope. d) Polar-dip, computing the plane or line of best fit between neighbouring points and outputs the minimum (red) and maximum (blue) magnitude of dip. e) Dip-steered minimum curvature, describing how bent a surface is at a particular point, measures the curve perpendicular to the maximum curvature and outputs its value (yellow). f) Dip-steered maximum curvature, measuring the maximum amount of bending orthogonal to the minimum curvature and outputs its value (yellow). g) Full-steered detailed similarity, a gently filtered attribute calculating and outputting the best likeness (black), and least likeness (white), between adjacent traces by following the dips and local azimuths of the time-slice in all directions at every trace position. h) Full-steered background similarity, a heavily filtered attribute calculating and outputting the best likeness (black), and least likeness (white), between adjacent traces by following the dips and local azimuths of the time-slice in all directions at every trace position. i) Non-steered similarity, calculating and outputting the best likeness (black), and least likeness (white), between adjacent traces without dip steering. j) Ridge enhancement filter, comparing in the time-slice domain three neighbouring similarity values in six different directions and outputs the largest ridge value (grey)..... 20

Figure 9: Ridge enhancement filter attribute comparison applied to a horizontal time-slice taken at 2172 ms in the Ship Shoal 3D seismic volume. a) The original ridge enhancement filter. b) Ridge enhancement filter and similarity attribute. 21

Figure 10: Salt diapirs within the Ship Shoal and North-West Gulf Coast 3D seismic volumes. a) Crossline 2190 of the Ship Shoal 3D seismic volume depicting diapir 1 (SS1). b) Crossline 2190 of the Ship Shoal 3D seismic volume depicting diapir 2 (SS2). c) Crossline 2190 of the Ship Shoal 3D seismic volume depicting diapir 3 (SS3). d) Inline 2167 of the Ship Shoal 3D seismic volume depicting diapir 4 (SS4). e) Crossline 3112 of the Ship Shoal 3D seismic volume depicting diapir 5 (SS5). f) Crossline 4570 depicting diapir 6 (NW1) within the North-West Gulf Coast 3D seismic volume. 22

Figure 11: A horizontal time-slice of the Ship Shoal 3D seismic volume at 1272 ms. The time-slice is overlain with the ridge enhancement filter and similarity attribute. Rose diagrams illustrate strike orientations of attribute features within salt diapirs, and surrounding sediment. 26

Figure 12: A horizontal time-slice of the Ship Shoal 3D seismic volume at 2800 ms. The time-slice is overlain with the ridge enhancement filter and similarity attribute. Rose diagrams illustrate strike orientations of attribute features within salt diapirs..... 27

Figure 13: Horizontal time-slices, and rose diagrams of attribute feature strike orientations within salt diapir NW1, from the North-West Gulf Coast 3D seismic volume displaying the ridge enhancement filter and similarity attribute. a) An upper time-slice taken at 2732 ms, and b) A lower time-slice taken at 3824 ms. 28

Figure 14: Crossline 3180 crosscutting a time-slice taken at 1272 ms from the Ship Shoal 3D seismic volume. The ridge enhancement filter and similarity attribute has been applied to time slice 1272. Crossline 3180 displays dip-steered amplitudes with mapped faults (white) and mapped fault projections displayed in green. 30

Figure 15: Behaviour of seismic attribute features and maximum horizontal stress (S_{Hmax}) orientations at varying lithological interfaces. a) Ridge enhancement filter and similarity attribute features displayed on a horizontal time-slice at 2800 ms. Attributes representing structural features in salt (blue) and deltaic sediment (orange) form parallel to the salt-sediment interface. b) Simplified schematic interpretation of A highlighting the analogous behaviours between attribute features within salt and deltaic sediment. c) Schematic illustration of S_{Hmax} directions and subsequent deflections when approaching zones of relatively harder or softer rock (Bell 1996)..... 33

Table 1: Attributes applied to the Ship Shoal and North-West Gulf Coast 3D seismic volumes and their functions..... 15

1. INTRODUCTION

Uncertainty exists as to the patterns of deformation that develop within active salt detachments beneath submarine fold-thrust belts. Large deltas exhibiting extensional faults are commonly linked to down-slope deep-water fold and thrust belts; described here as delta and deep-water fold-thrust belts (DDWFTBs). Deformation is accommodated by one or more detachment zones, generally a pro-delta shale or salt (Yassir and Zerwer 1997, Rowan et al. 2004, Morley et al. 2011). Present-day active detachment zones are often located in inaccessible submarine regions (Hansberry et al. 2014). As a result, basal detachments deformed in active fold and thrust belts are poorly understood.

Salt deformed within DDWFTBs is currently viewed as a viscous substrate, exhibiting ductile deformation beneath a brittle, mechanically detached sedimentary overburden (e.g. Coward and Stewart 1995, Davison et al. 1996, McClay et al. 2003, Mourgues and Cobbold 2006, Krézsek et al. 2007). However, outcrop studies by Richards et al (2014) have shown that salt deformed within fold and thrust belts exhibits brittle deformation.

Past studies of the Gulf of Mexico have utilised seismic amplitude data to identify and interpret salt-sediment interactions (e.g. Wu et al. 1990, Jackson et al. 1994, Rowan 1997, Hudec et al. 2013a, Hudec et al. 2013b). Seismic amplitude studies are an effective tool for basin analysis; however, there are lower limits to seismic amplitude resolution that preclude the detection of small-scale features (Roberts 2001, Backé et al. 2012). Fortunately, techniques to improve the detection of sub-seismic amplitude

geological features are available, such as seismic attribute calculation and analysis (e.g. Hesthammer and Fossen 1997, Chopra and Marfurt 2005, Iacopini and Butler 2011, Backé et al. 2012). In this study, structural fabrics that lie below the detection threshold of seismic amplitude data will be identified and mapped by seismic attribute analysis. Analysis will take place within two 3D seismic volumes, with focus on the detachment surface and surrounding sedimentary overburden.

2. BACKGROUND

2.1 The Gulf of Mexico

The Gulf of Mexico is a small oceanic basin located between the North American continent and the Yucatán Peninsula (Figure 1a, Salvador 1987, Yassir and Zerwer 1997, Galloway et al. 2000). Opening of the Gulf of Mexico was initiated by continental rotation and crustal extension of the Yucatán Peninsula (ca. 160-150 Ma, Bird et al. 2005). The northern rim of the Gulf of Mexico is a passive continental margin, dominated by Triassic to Early Jurassic NE-SW striking listric growth faults (Figure 1a and 1b, Salvador 1987, Marton and Buffler 1999). During the Middle-Late Jurassic, tectonic subsidence rates and stratigraphic base level were high in the northern Gulf, resulting in the production of substantial accommodation space for sediment accumulation (Nunn 1984, Sawyer et al. 1991). The resulting Jurassic through Holocene strata accumulated as part of a seaward-dipping sedimentary wedge, and was deposited in differentially subsiding basins in the developing Gulf of Mexico (Figure 1b, Martin 1978, Trudgill et al. 1999).

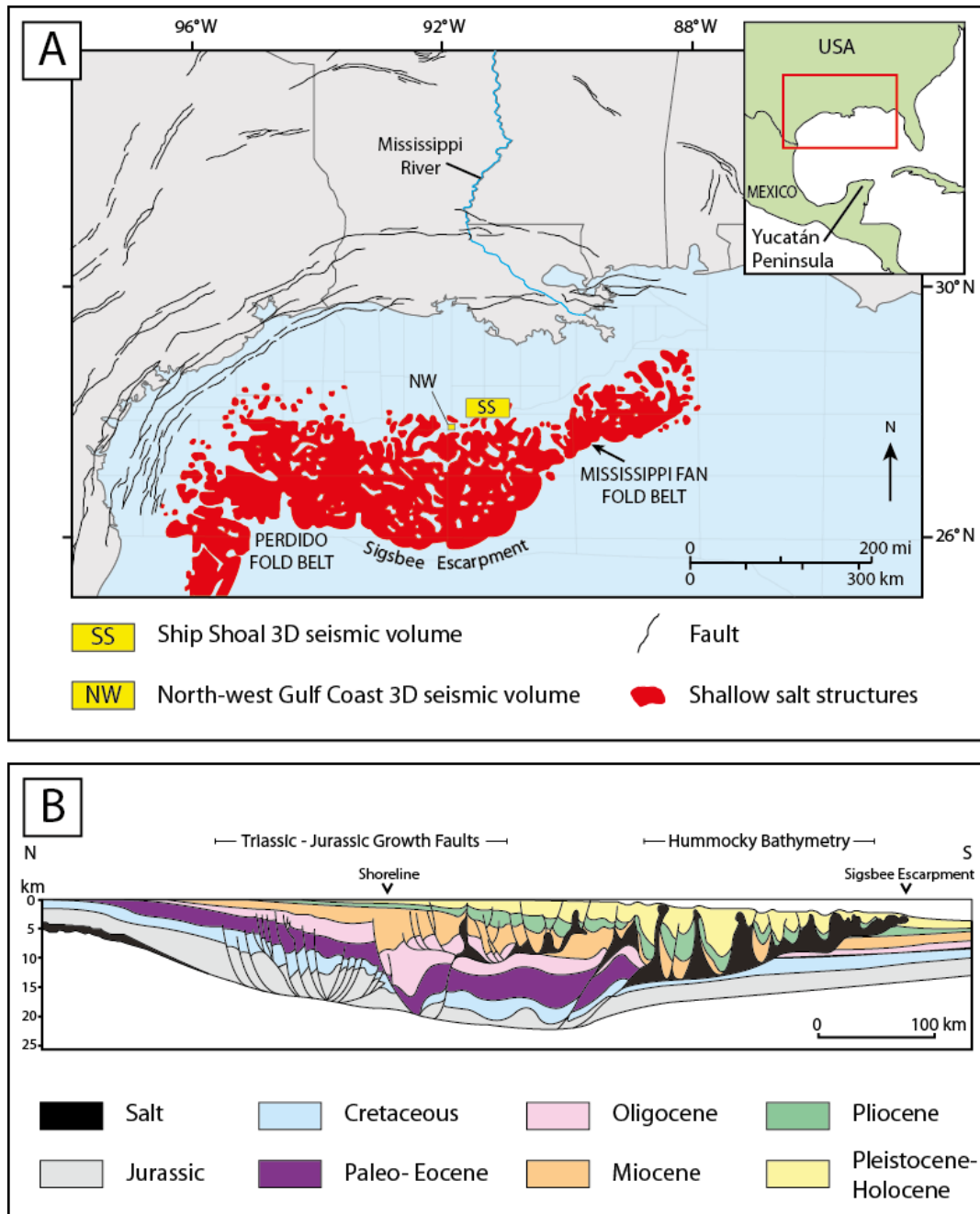


Figure 1: a) Location map of the northern Gulf of Mexico basin illustrating the locations of the Ship Shoal and North-West Gulf Coast 3D seismic volumes (modified from Hudec et al. 2013a). b) Generalised cross-section of the northern Gulf of Mexico basin displaying stratigraphy and structural elements. Stratigraphy within the northern Gulf consists of a succession of Jurassic through Holocene strata (modified from Galloway 2008).

Intermittent influx of seawater and subsidence-driven marine transgression led to the deposition of the Jurassic age Louann Salt over Mexico and the southern United States of America (Wilhelm and Ewing 1972, Jackson and Seni 1983). The allochthonous Louann Salt is most prevalent in the north of the Gulf of Mexico, and is a source of extensive diapirism (Jackson et al. 1994). Although not widespread, smaller salt sheets lie above the Louann Salt (Rowan and Vendeville 2006). The formation of these salt sheets was result of continued rapid sediment accumulation during the Neogene, resulting in down-dip spreading and over-thrusting of salt within unconsolidated sediment (Wu et al. 1990). The Louann Salt lies stratigraphically below the overlying deltaic sediments, and acts as a regional detachment zone (Wu et al. 1990). As a result, continuous progradation of the overlying sediment has led to the formation of Perdido and Mississippi Fan Fold Belts (Figure 1a, Trudgill et al. 1999).

2.2 Delta and Deep-Water Fold-Thrust Belts in the Gulf of Mexico

Delta and deep-water fold-thrust belts are linked systems of extension and compression that are typically the result of far-field stresses, near field stresses, or a combination of both (Yassir and Zerwer 1997, King and Backé 2010, Morley et al. 2011). Gravitational failure of deltaic sediment along a continental slope results in an extensional regime at the delta-top that drives a down-dip compressional regime in the delta toe (Figure 2, Rowan et al. 2004, King et al. 2009). Deformation is constrained above a weak basal layer or detachment zone, where extensional listric normal faults form at the delta top, and are accompanied by compression driven thrust faulting in the delta toe (Davis and Engelder 1985, Rowan 1997, McClay et al. 2003). Down-dip of the delta top is a transitional zone subject to regional thin-skinned extension (Figure 2). The zone is

characterised by extensive diapirism below extensional fault structures, such as grabens and half grabens (Vendeville and Jackson 1992b).

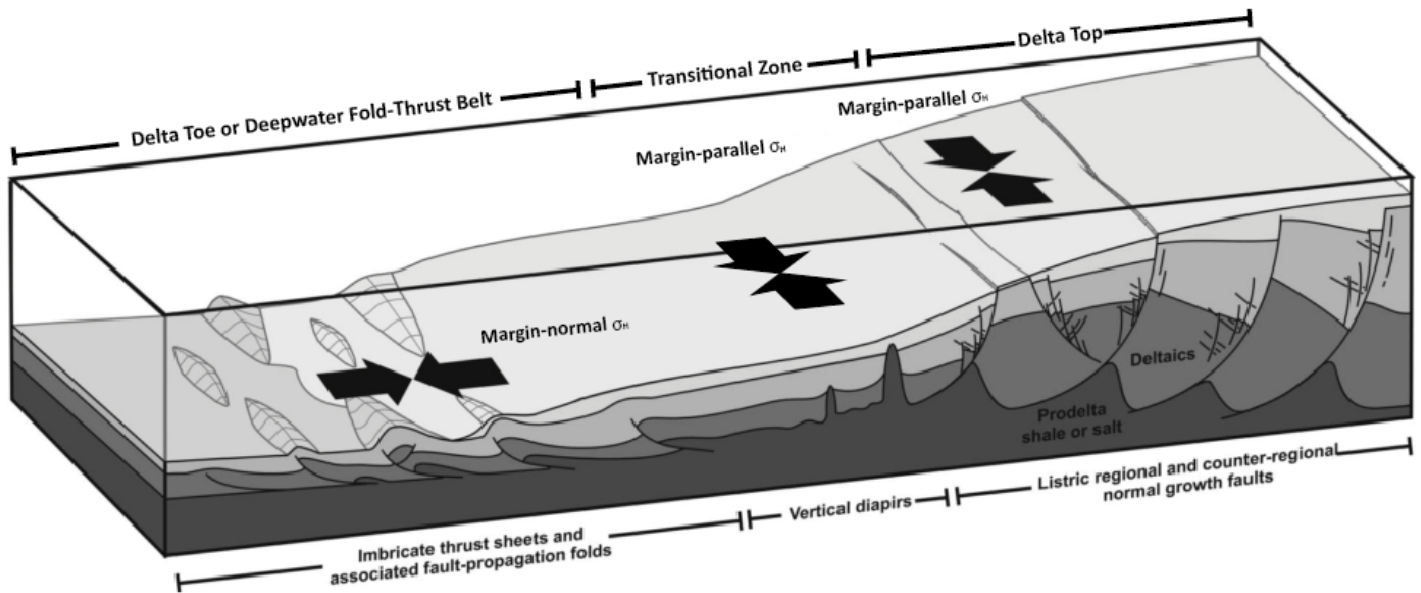


Figure 2: Schematic model of a delta and deep-water fold-thrust belt demonstrating a 90° rotation of maximum horizontal stress (σ_H) from margin parallel to margin normal, respectively (King et al. 2009). Normal listric growth faults form due to extension at the delta-top. Thin-skinned extension dominates the transitional zone accommodating salt and shale diapirism. Stacked thrust sheets with associated folds occur at the distal pinch-out of the detachment, forming the delta toe (modified from King and Backé 2010).

Deep-water fold-thrust belts can be classified into two types of systems. Type 1 systems have either a weak shale or salt detachment and predominantly occur on passive margins (Morley et al. 2011). Type 2 systems are deformed by either far-field stress alone, or mixed near- and far-field stress. Type 2 systems are subdivided on a tectonic basis into continent convergence zones and active margin deep-water fold thrust belts (Morley et al. 2011). Within the Gulf of Mexico, the Mississippi Fan and Perdido Fold Belts are classified as near-field stress driven Type 1 systems.

2.3 Properties of Salt and Salt Structures

2.3.1 PROPERTIES OF SALT

Salt is considered as a viscous material with the ability to flow when subjected to minimal shear stresses, due its very low strength (Urai et al. 1986, Morley and Guerin 1996, Davison et al. 1996, Rowan et al. 2004). Salt is almost incompressible, and is particularly weak at low temperatures and pressures, such as those in DDWFTBs (Davis and Engelder 1985). Salt deposits are heterogeneous in nature, and will often consist of interbedded sedimentary or carbonate sequences (Warren 2006).

Deformation of salt layers occurs by means of Poiseuille and Couette flow (Figure 3, Jaeger and Neville 1979). Poiseuille flow is associated with the vertical thinning and lateral expulsion of evaporite layers, where flow is restricted by the viscous shear forces along the boundaries of the salt, or interbedded sedimentary sequences (Figure 3a, Davison et al. 1996, Rowan et al. 2004, Fossen 2010). Couette flow exhibits simple shear within the salt layer, as the overburden is translated relative to the substrate (Figure 3b, Davison et al. 1996, Rowan et al. 2004, Fossen 2010).

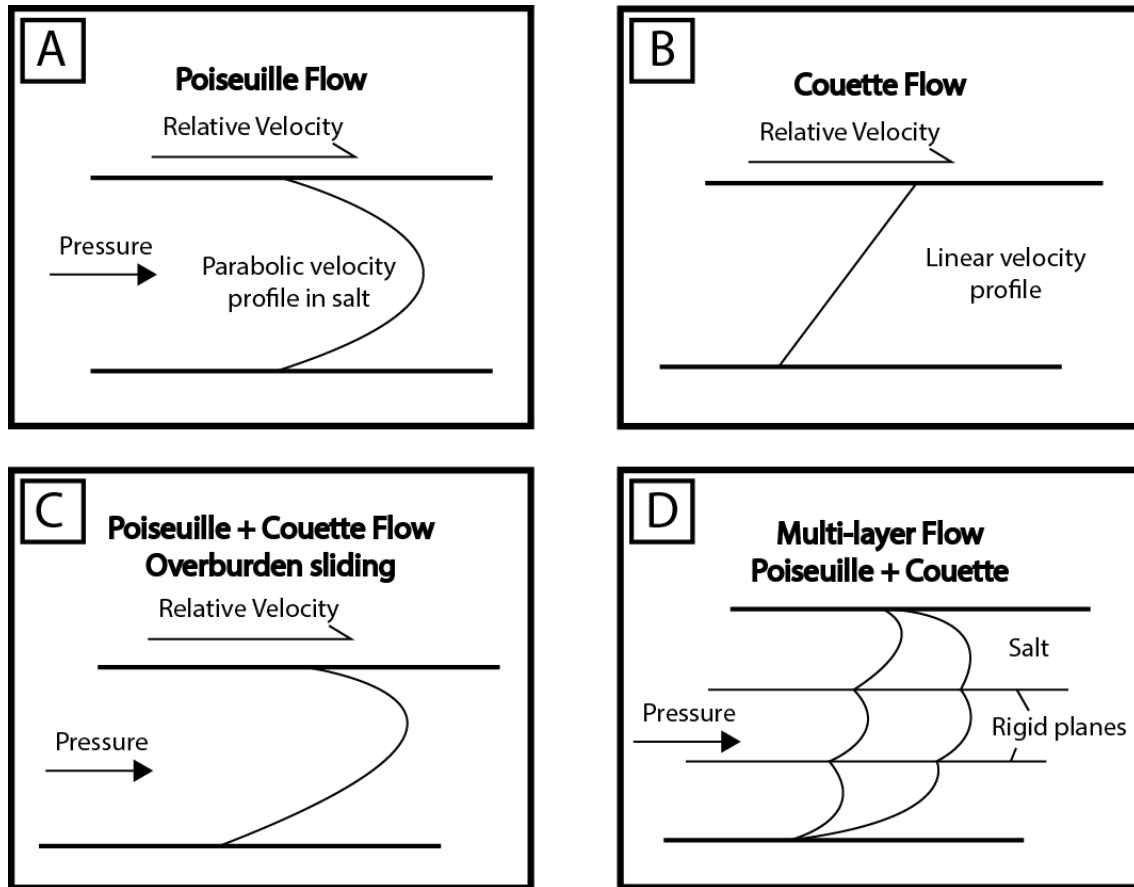


Figure 3: Schematic illustration of salt velocity profiles. a) Poiseuille flow in a single thick layer. b) Couette flow produced by overburden sliding. c) Combination of Poiseuille and Couette flow, displaying relative movement along resistive bounding layers. d) Poiseuille and Couette flow across multiple layers, where interbedded sequences form rigid planes (modified from Davison et al. 1996).

2.3.2 SALT DIAPIRS

Salt diapirs have been identified and extensively studied within the Gulf of Mexico (e.g. Salvador 1987, Bouma and Roberts 1990, Yassir and Zerwer 1997, Bird et al. 2005, Hudec et al. 2013a). Diapirs within the Gulf of Mexico have discordant contacts with their encasing sediments and form from buoyant uplift beneath denser strata (Jackson and Talbot 1986, Marsh 2008). Diapir evolution varies between structural settings and can be separated into reactive, active and passive diapirism (Figure 4, Vendeville and Jackson 1992a, Vendeville and Jackson 1992b).

During extensional faulting, reactive diapirism will occur during the initial stages of diapir growth, where salt pierces the overburden due to differential loading imposed by the overlying graben (Jackson et al. 1994). The growth of a reactive diapir is controlled by the amount of regional extension. The greater the amount of extension, the taller the diapir (Vendeville and Jackson 1992b). Reactive diapirs are most commonly found in thin overburdens within the lower extensional zone, or in areas responding to tectonic strain (Vendeville and Jackson 1992a, Jackson et al. 1994, Marsh 2008, Fossen 2010).

Active diapirs often proceed reactive diapirism and pierce the overlying sediments by lifting and thrusting aside tectonically thinned overburden (Jackson et al. 1994). The salt pierces in increments and can only occur when the roof overlying the salt is sufficiently thin (Morley and Guerin 1996).

Once a diapir has emerged at the surface it becomes passive and is expelled laterally on top of the sediments (Morley and Guerin 1996). Throughout its growth a passive diapir will experience downbuilding; where the base of the salt sinks along with the adjoining sediments (Jackson et al. 1994). A passive diapir will narrow upwards if the rate of sedimentation exceeds the rate of net salt rise, and will widen if sedimentation is lower than diapiric rise (Jackson et al. 1994, Davison et al. 1996).

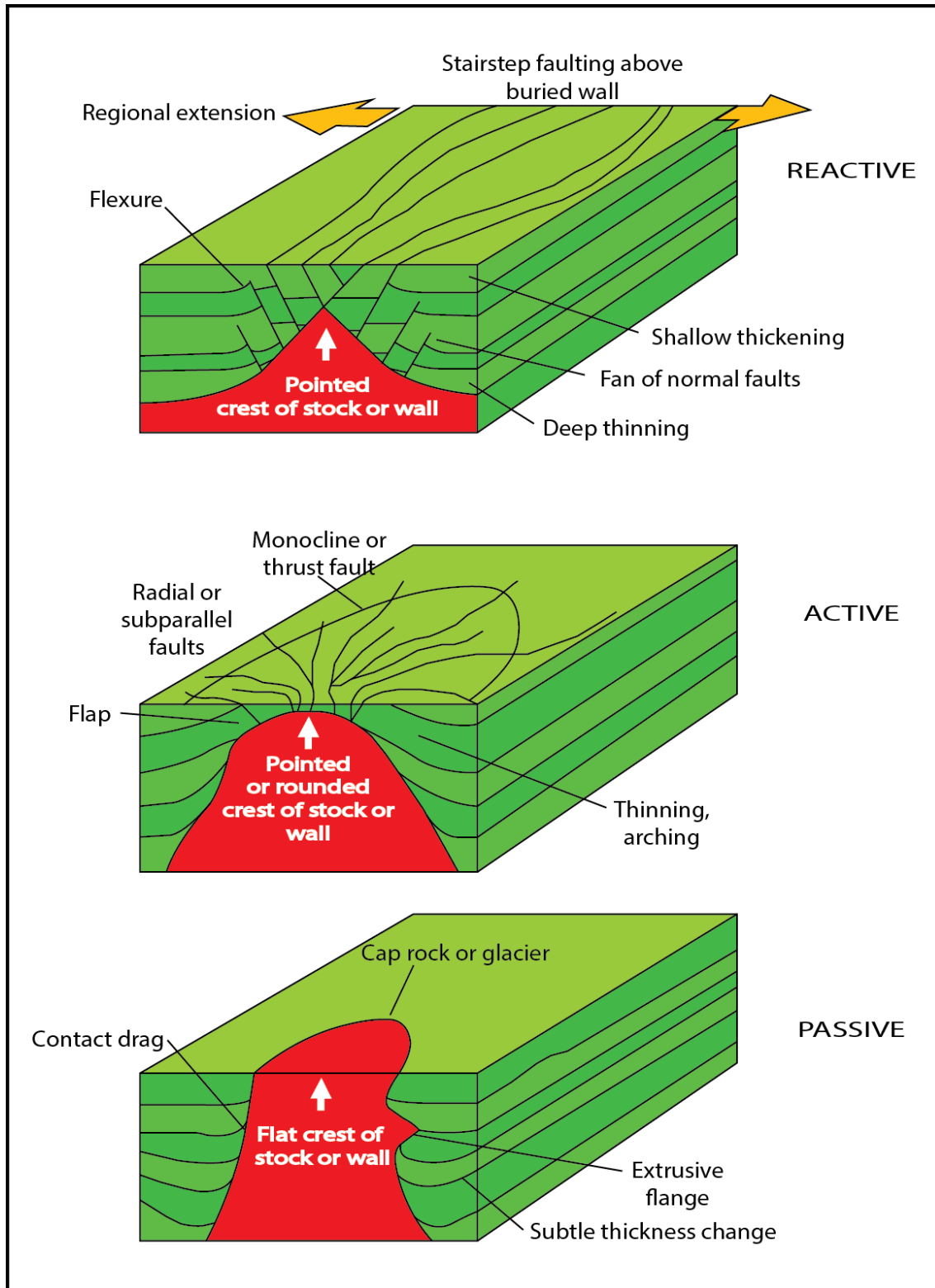


Figure 4: Three modes of salt diapirism and their characteristic structures. A reactive diapir displaying a fan of normal faults along its flanks with associated flexure of sediments. An active diapir below a radial network of faults. A passive diapir displaying near-vertical flank geometry and associated dragging of sediments (modified from Jackson et al. 1994).

2.4 Analogue Models of Salt Detachments and Structures

Analogue models are an effective tool in investigating the brittle and ductile deformation of salt detachments and structures. Modern physical models commonly use a two-layer system consisting of sand and silicone (Brun et al. 1994). Silica (quartz) sand is used in a number of studies to replicate brittle sediments (e.g. Bahroudi and Koyi 2003, Rowan and Vendeville 2006, Krézsek et al. 2007).

For diapirism to occur within a physical model, the detachment surface must consist of a low-density medium. The majority of detachment surfaces within analogue models are made up of a viscous silicone polymer, or low-density equivalent, forming a thin ductile décollement (i.e. Bahroudi and Koyi 2003, Rowan and Vendeville 2006, Krézsek et al. 2007). Results from physical models aim to identify a range of structural mechanics, including understanding overburden deformation related to diapirism and structural patterns exhibited by salt detached fold and thrust belts (Alsop 1996, Krézsek et al. 2007).

However, physical models using layered sand overburdens possess an unrealistically high initial density ratio between overburden and salt (Dooley et al. 2007). Models using overburdens consisting entirely of sand have a density ratio that is more than five times higher than in nature (Dooley et al. 2007). Dooley et al. (2007) uses a combination of silica sand with alternating layers of hollow glass beads, reducing the bulk density of the modelled overburden.

Further limitations exist when modelling the detachment where analogue materials do not mimic the detachment lithologies in nature (Back et al. 2008). Modelled salt detachments consisting of viscous substances restrict the observable deformation style to plastic processes. Due to the submarine nature of active salt detachments, deformation styles within fold-thrust belts are still relatively unknown, and may therefore not be accurately demonstrated by a viscous medium (Cohen and McClay 1996).

3. METHODS

3.1 Seismic Data Sets

Seismic data has been used extensively in the study of subsurface salt structures by a number of authors (e.g. Wu et al. 1990, Morley and Guerin 1996, Treviño and Vendeville 2008). In this study, the Ship Shoal and North-West Gulf Coast 3D seismic volumes from the Gulf of Mexico have been used to investigate the deformation of the Louann Salt detachment. The larger Ship Shoal 3D seismic volume covers 7,766.418 km² and is located northeast of the Perdido Fold Belt and west of the Mississippi Fan Fold Belt (Figure 1a). Situated southwest of the Ship Shoal 3D seismic volume is the smaller North-West Gulf Coast 3D seismic volume. This survey lies northeast of the Perdido Fold Belt and covers 981.294 km² (Figure 1a).

3.2 Data Quality

Seismic imaging within salt tectonics often results in poor reflection data and distortion of surrounding strata. Salt boundaries can be delimited by strong reflectivity, but are

more often characterised by a change in the seismic texture (Figure 5, Ratcliff et al. 1992, Sava and Biondi 2004, Berthelot et al. 2013).

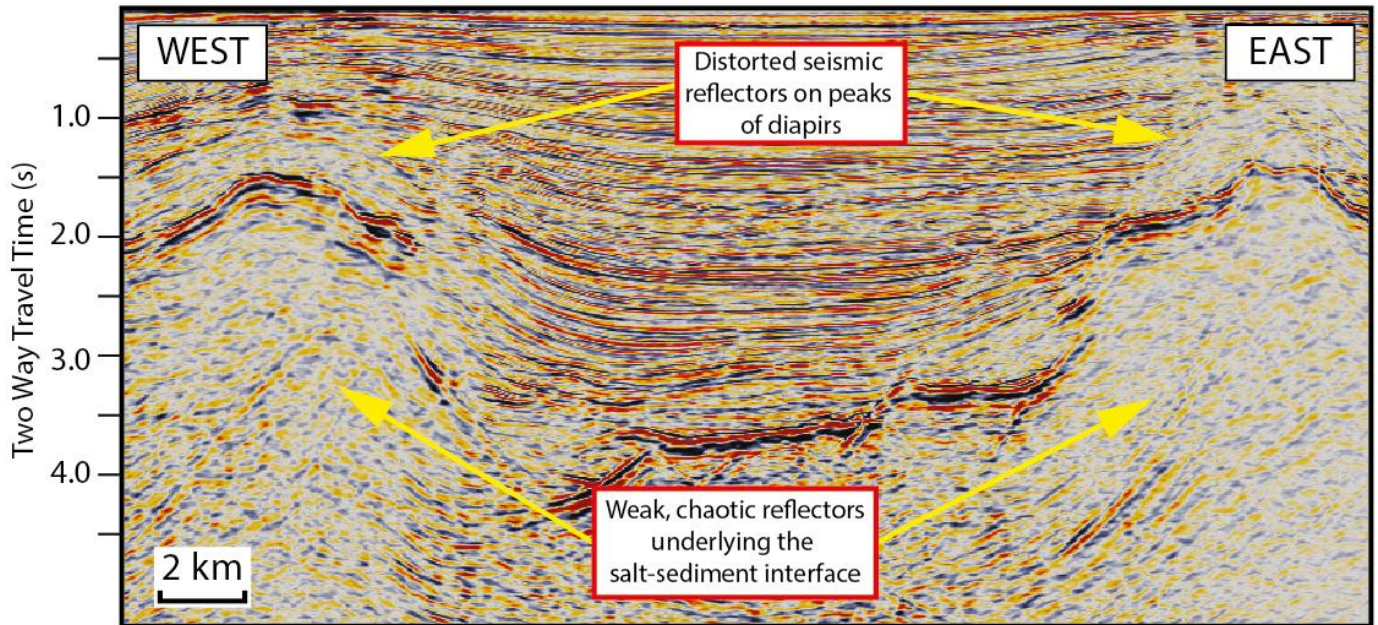


Figure 5: Crossline 2190 of the Ship Shoal seismic volume illustrating the distortion of amplitude velocities imposed by salt. The top layer of salt is identified by strong reflectivity.

To improve the quality of the raw seismic data each 3D survey was subject to a dip-steered median filter. Steering a seismic volume can improve the detection and interpretation of faults and fractures (Stewart 1985, Backé et al. 2012, Chehrazi et al. 2013). In a dip-steering calculation, amplitude dip directions are stored, providing a measure of continuity and structure of seismic events (de Rooij and Tingdahl 2002). The dip information stored in the data volume is then used to simulate a virtual horizon at each position (Backé et al. 2012). This allows for the decrease of random noise in the data volume and, when combined with a median filter, enhances lateral continuous seismic events (Marfurt et al. 1998b). In median filtering, the centre amplitude value of a dip-steered area is replaced by the median amplitude of the extracted volume. The

result is an edge-preserving smoothing of the seismic data (Marfurt et al. 1998b, Backé et al. 2012).

3.3 Seismic Interpretation

Within the full coverage of the Ship Shoal and North-West Gulf Coast 3D seismic volumes six antiformal structures were identified and interpreted as salt diapirs.

Amplitudes displaying strong reflectivity along the tops of the antiforms were identified as the top salt layer (Figure 6). Dissimilar styles of seismic amplitudes above and below the interpreted top salt layer represented a change in lithology (Ratcliff et al. 1992, Sava and Biondi 2004). Above the top salt; strong, regularly alternating amplitudes were interpreted as deltaic deposits. Diffuse reflectors below the top salt layer were interpreted as the remaining salt body. Linear offsets of amplitudes were abundant in the Ship Shoal deltaic deposits and were interpreted as normal and reverse faults, relative to their direction of offset.

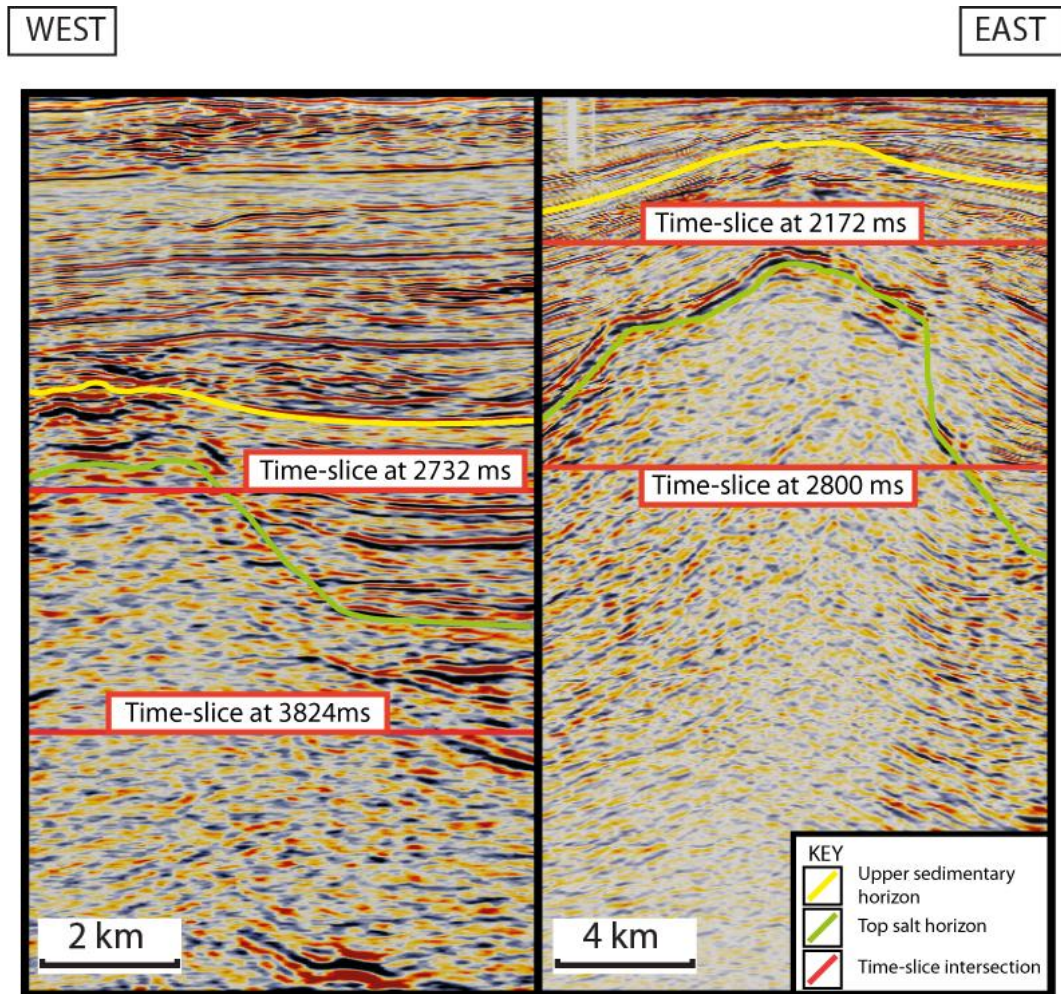


Figure 6: Interpretation areas Crosslines 4842 from the North-West Gulf Coast and 2190 from the Ship Shoal 3D seismic volume containing time-slices and interpreted horizons. A) Interpreted horizons representing the top salt layer and an upper sedimentary horizon, along with time-slices taken at 2732 and 3824 ms (North-West Gulf Coast seismic volume). B) Interpreted horizons representing the top salt layer and an upper sedimentary horizon, along with time-slices taken at 2172 and 2800 ms (Ship Shoal seismic volume).

Interpretation was focussed on two mapped horizons and two horizontal time slices in each survey area (Figure 6). Firstly, the top salt layer from each survey was picked and mapped, providing a three-dimensional view of the geometry of each diapir. A second horizon was mapped immediately above the crest of the salt diapirs. This horizon demonstrated the effects of diapirism on overlying sedimentary layers.

3.4 Seismic Attributes

Seismic attribute analysis uses variations in the amplitudes of the seismic wavelet and tracks these through entire data volumes (Weimer and Davis 1996). This approach uses more of the signal than simple amplitude displays, and can greatly enhance the imaging of geological features (Bahorich and Farmer 1995a, Weimer and Davis 1996). In general, seismic attributes improve the signal interpretation of entire 3D seismic volumes (Weimer and Davis 1996). In this study, several seismic attributes are applied to the two 3D seismic volumes, including dip, azimuth, curvature, similarity and ridge enhancement filter attributes (Table 1).

Table 1: Attributes applied to the Ship Shoal and North-West Gulf Coast 3D seismic volumes and their functions.

ATTRIBUTES	FUNCTION
Dip (Polar Dip)	Displays a robust estimation of reflector convergence, divergence, parallelism or disorder, and delineates faults with offsets significantly less than the width of the seismic wavelet (Chopra and Marfurt 2007a, Backé et al. 2012).
Azimuth (Dip Azimuth)	Subtracts noise patterns or enhances seismic events and improves the signal-to-noise ratio in poor quality datasets (Chopra and Marfurt 2007a).
Curvature	Measures the direction of maximum and minimum curvature along the horizons azimuth (dip) direction. Curvature attributes image features below the resolution of seismic data, such as faults and fractures (Chopra and Marfurt 2007c).
Similarity	Seismic similarity is a measure of lateral continuity, and Identifies abrupt mismatches in amplitude along reflectors representing variations in structure, stratigraphy and lithology (Tingdahl et al. 2001).
Ridge Enhancement Filter	Detects the largest ridge values around a particular point. Highlighted values are representative of high angle folds, faults or fractures (Crutchley et al. 2011, Chehrazi et al. 2013).

Post application, a thorough visual evaluation was employed to identify which attributes were best represented in seismic displays (Figures 7 & 8). The dip-azimuth, polar-dip and non-steered similarity attributes were marginalised as they produced low resolution outputs, where adjacent features could not be identified (Figures 7c, d, i & 8c, d, i). The minimum-curvature attribute was also disregarded as attribute features displayed poor lateral continuity (Figures 7e & 8e). Attributes outputting high resolution of features included the maximum-curvature, ridge enhancement filter and full-steered similarity attributes (Figures 7f, g, h, j & 8f, g, h, j). Of these, the ridge enhancement filter attribute was selected for further analysis of the salt detachment, as it shows the highest level of detail (Figures 7j & 8j).

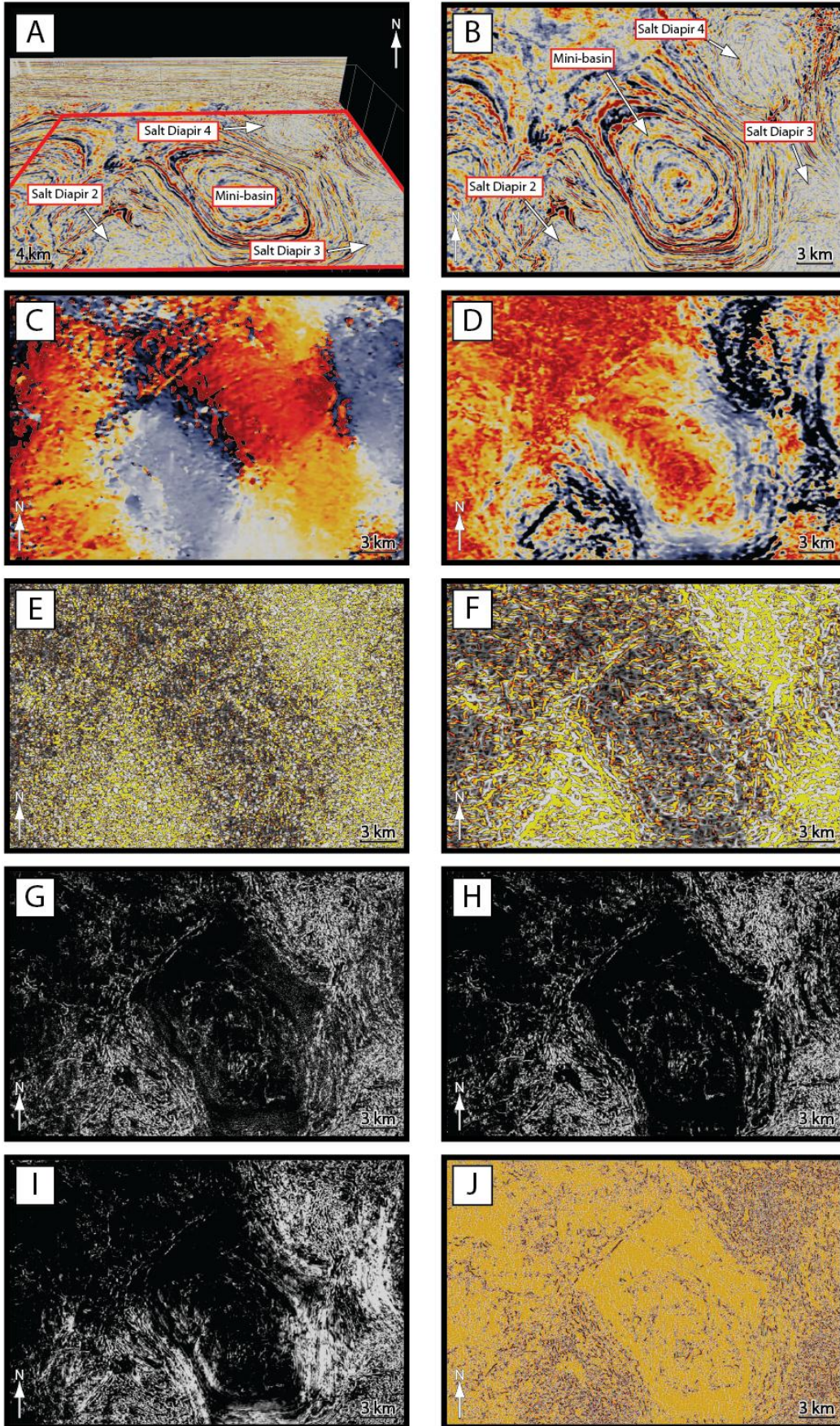


Figure 7: Different seismic attributes displayed on a horizontal time-slice at 1940 ms across the Ship Shoal 3D seismic volume in the Gulf of Mexico. a) Oblique view of time-slice 1940 intersecting crossline 2190 with interpreted structural features. b) Time-slice at 1940 ms of dip-steered median filtered seismic, removing random noise and enhancing laterally continuous seismic events by filtering along the structural dip. c) Dip- azimuth, computing the plane of best fit between neighbouring points and outputting the minimum (red) and maximum (blue) slope. d) Polar-dip, computing the plane or line of best fit between neighbouring points and outputs the minimum (red) and maximum (blue) magnitude of dip. e) Dip-steered minimum curvature, describing how bent a surface is at a particular point, measures the curve perpendicular to the maximum curvature and outputs its value (yellow). f) Dip-steered maximum curvature, measuring the maximum amount of bending orthogonal to the minimum curvature and outputs its value (yellow). g) Full-steered detailed similarity, a gently filtered attribute calculating and outputting the best likeness (black), and least likeness (white), between adjacent traces by following the dips and local azimuths of the time-slice in all directions at every trace position. h) Full-steered background similarity, a heavily filtered attribute calculating and outputting the best likeness (black), and least likeness (white), between adjacent traces by following the dips and local azimuths of the time-slice in all directions at every trace position. i) Non-steered similarity, calculating and outputting the best likeness (black), and least likeness (white), between adjacent traces without dip-steering. j) Ridge enhancement filter, comparing in the time-slice domain three neighbouring similarity values in six different directions and outputs the largest ridge value (grey).

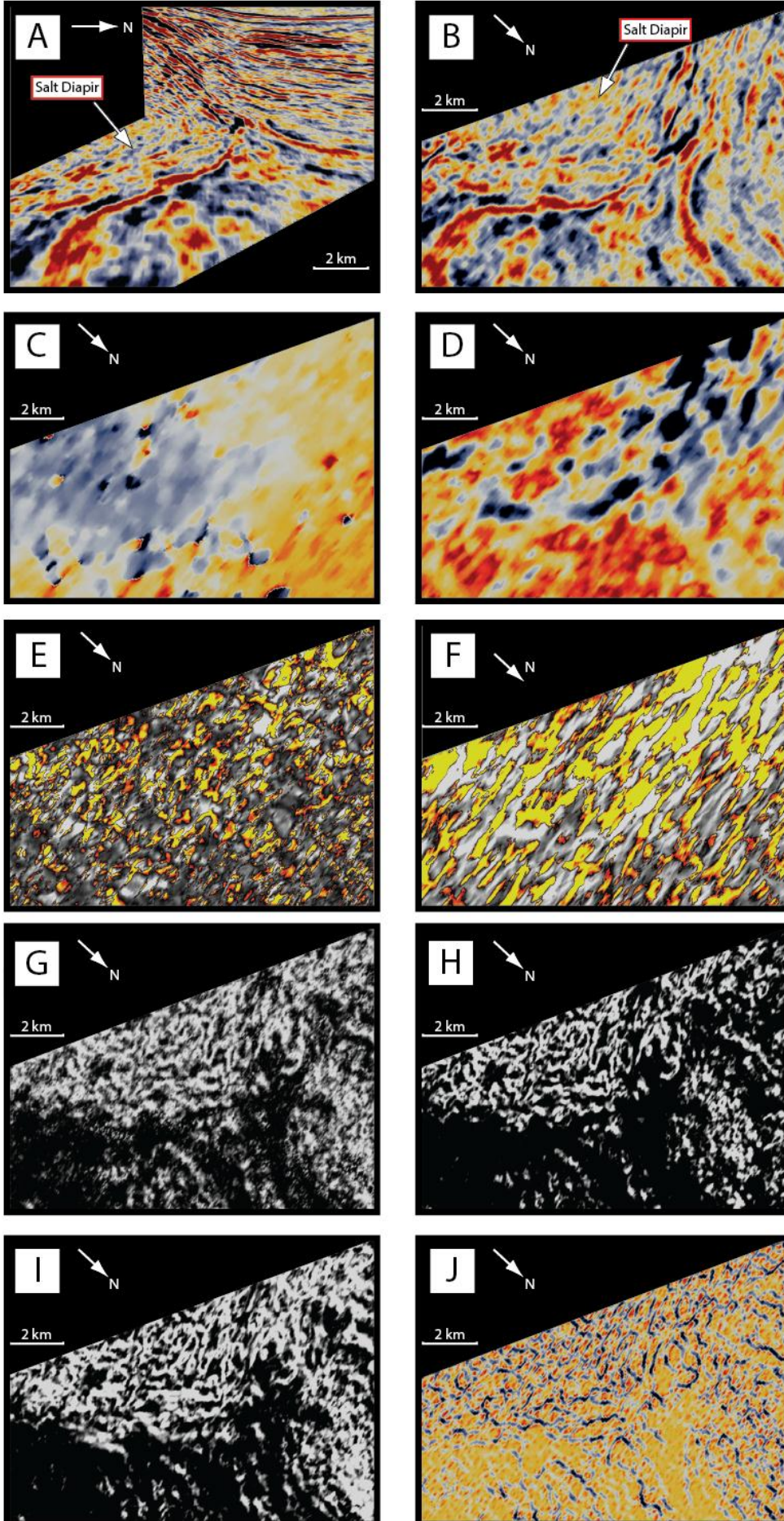


Figure 8: Different seismic attributes displayed on a horizontal time-slice at 2928 ms across the North-West Gulf Coast 3D seismic volume in the Gulf of Mexico. a) Oblique view of the intersection between time-slice 2928 and crossline 4570 with an interpreted salt diapir. b) Time-slice at 2928 ms of dip-steered median filtered amplitudes, removing random noise and enhancing lateral continuous seismic events by filtering along the structural dip. c) Dip- azimuth, computing the plane of best fit between neighbouring points and outputting the minimum (red) and maximum (blue) slope. d) Polar-dip, computing the plane or line of best fit between neighbouring points and outputs the minimum (red) and maximum (blue) magnitude of dip. e) Dip-steered minimum curvature, describing how bent a surface is at a particular point, measures the curve perpendicular to the maximum curvature and outputs its value (yellow). f) Dip-steered maximum curvature, measuring the maximum amount of bending orthogonal to the minimum curvature and outputs its value (yellow). g) Full-steered detailed similarity, a gently filtered attribute calculating and outputting the best likeness (black), and least likeness (white), between adjacent traces by following the dips and local azimuths of the time-slice in all directions at every trace position. h) Full-steered background similarity, a heavily filtered attribute calculating and outputting the best likeness (black), and least likeness (white), between adjacent traces by following the dips and local azimuths of the time-slice in all directions at every trace position. i) Non-steered similarity, calculating and outputting the best likeness (black), and least likeness (white), between adjacent traces without dip steering. j) Ridge enhancement filter, comparing in the time-slice domain three neighbouring similarity values in six different directions and outputs the largest ridge value (grey).

However, close inspection of time-slices containing the ridge enhancement filter attribute displayed chaotic values within interpreted salt structures (Figures 7j and 8j). To improve attribute representation within these structures the smaller anomalous ridge enhancement filter values were removed by raising the detection threshold during attribute calculation (Appendix A). While smaller attribute features were responsible for considerable noise they also contributed to the continuity of attribute arrangements. To amend their absence, the optimised ridge enhancement filter attribute was overlain onto the full-steered similarity attribute using a technique described by Francelino and Antunes (Figure 9, 2013).

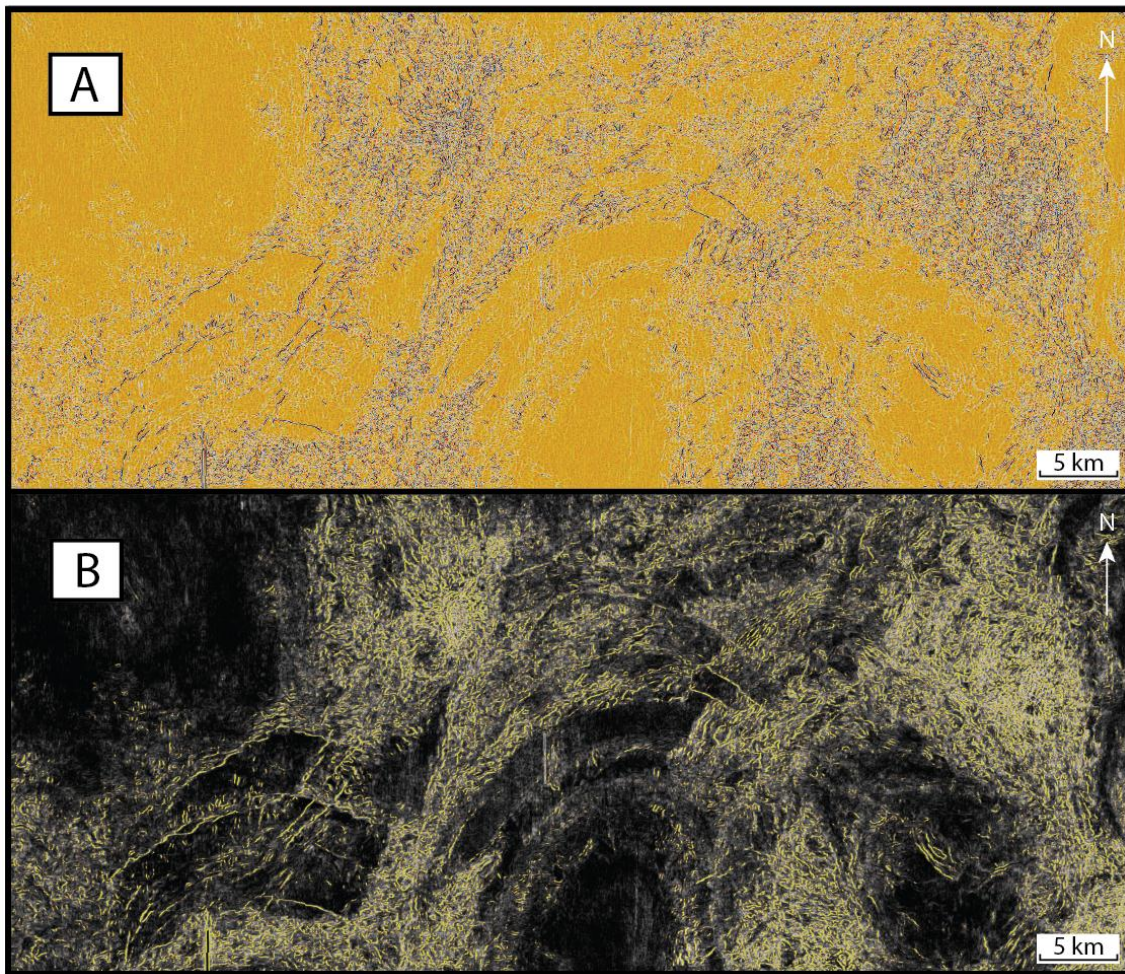


Figure 9: Ridge enhancement filter attribute comparison applied to a horizontal time-slice taken at 2172 ms in the Ship Shoal 3D seismic volume. a) The original ridge enhancement filter. b) Ridge enhancement filter and similarity attribute.

4. SALT DIAPIRS IDENTIFIED IN THE GULF OF MEXICO

Classification of salt diapirs within the Ship Shoal and North-West Gulf Coast 3D seismic volumes was based on a study by Jackson (1994), and was founded on diapir geometry and surrounding structural features within the sedimentary overburden (Figure 10). Seismic interpretation focussed on the top salt and the overlying sedimentary overburden. The purpose of interpretation was to identify structural features visible

within the seismic volume to allow further investigation using seismic attribute analysis. The six diapirs identified by seismic interpretation have been named SS1, SS2, SS3, SS4, SS5 and NW1, respectively.

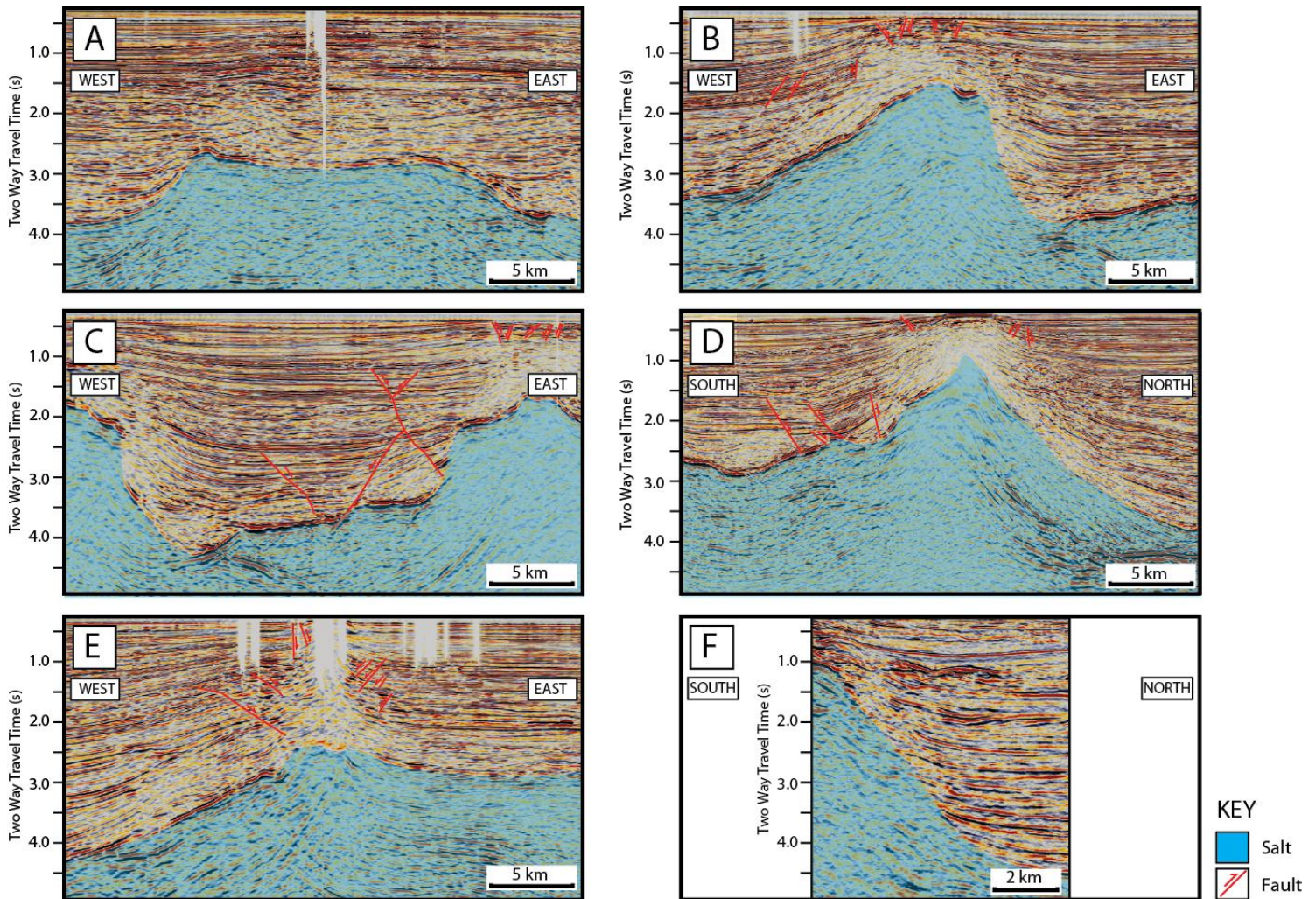


Figure 10: Salt diapirs within the Ship Shoal and North-West Gulf Coast 3D seismic volumes. a) Crossline 2190 of the Ship Shoal 3D seismic volume depicting diapor 1 (SS1). b) Crossline 2190 of the Ship Shoal 3D seismic volume depicting diapor 2 (SS2). c) Crossline 2190 of the Ship Shoal 3D seismic volume depicting diapor 3 (SS3). d) Inline 2167 of the Ship Shoal 3D seismic volume depicting diapor 4 (SS4). e) Crossline 3112 of the Ship Shoal 3D seismic volume depicting diapor 5 (SS5). f) Crossline 4570 depicting diapor 6 (NW1) within the North-West Gulf Coast 3D seismic volume.

4.1 SS1

SS1 is interpreted to have actively risen through the overlying sediment (Figure 10a). It is implied that after the initial reactive diapir event, collapse occurred from the expulsion of underlying salt. An active phase of diapirism is then interpreted to have occurred, and is supported by the rounded crest of the salt diapir.

4.2 SS2

SS2 is interpreted to have actively risen through the overlying sediment (Figure 10b). The diapir's rounded crest of stock underlies a set of sub-parallel faults, indicating active diapirism. Further evidence is observed between 0 - 1 s (TWT), where deltaic sediment beds thin towards the diapir.

4.3 SS3

SS3 is interpreted to have reactively pierced through the overlying sediments, with subsequent phases of active and passive diapirism (Figure 10c). The diapir itself shows early signs of diapiric collapse about its semi-rounded crest at 1 s (TWT), observed on its west and eastern flanks. Reactive diapirism is strongly supported by the presence of deep thinning (2.5 s) and shallow thickening (1.5 s) of the surrounding deltaic sediments. Additionally, the presence of normal faults flanking the diapir's western flank is another indication of reactive diapirism.

4.4 SS4

SS4 is interpreted to have reactively pierced the overlying sediment (Figure 10d). Evidence for reactive diapirism lies in the diapir's pointed crest of stock, fan of flanking

normal faults (southern flank) and flexure of foot and hanging walls observed between them.

4.5 SS5

SS5 is interpreted to have reactively pierced the overlying sediment (Figure 10e). The diapirs pointed crest of stock and adjacent fan normal faults along the diapirs flanks are a result of reactive diapirism. Shallow thickening of sedimentary layers is observed at 0.5 s (TWT), where faulted blocks positioned directly above the diapir are thicker than those surrounding them. Deep thinning of deltaic sediments are also observed on the western flank at 2.5 s (TWT).

4.6 NW1

NW1 is interpreted to have actively risen through the overlying deltaic sediments (Figure 10f). The diapir has a rounded crest of stock, and displays characteristic thinning of sediments up and along its northern flank.

5. SEISMIC ATTRIBUTE ANALYSIS

The combined ridge enhancement filter and similarity attribute was applied to two upper and two lower horizontal time-slices; at 1272/2800 ms for the Ship Shoal seismic cube, and at 2732/ 3824 ms for the North-West Gulf Coast seismic cube (Figures 11, 12 and 13). Each time-slice was overlain with the previously interpreted 3D top salt horizon with intersections delineating the salt-sediment interface, constraining the lateral extent of the six previously interpreted diapirs. Rose diagrams were constructed from the strike orientations of attributes features (Figures 11, 12 and 13). Within the lower-time slices strike orientations were taken from inside the protruding salt diapirs. However, within the upper time-slices, the lesser exposure of protruding diapirs throughout the time-slice resulted in strike orientations being recorded from inside salt diapirs and the surrounding sediment in a 5 km radius.

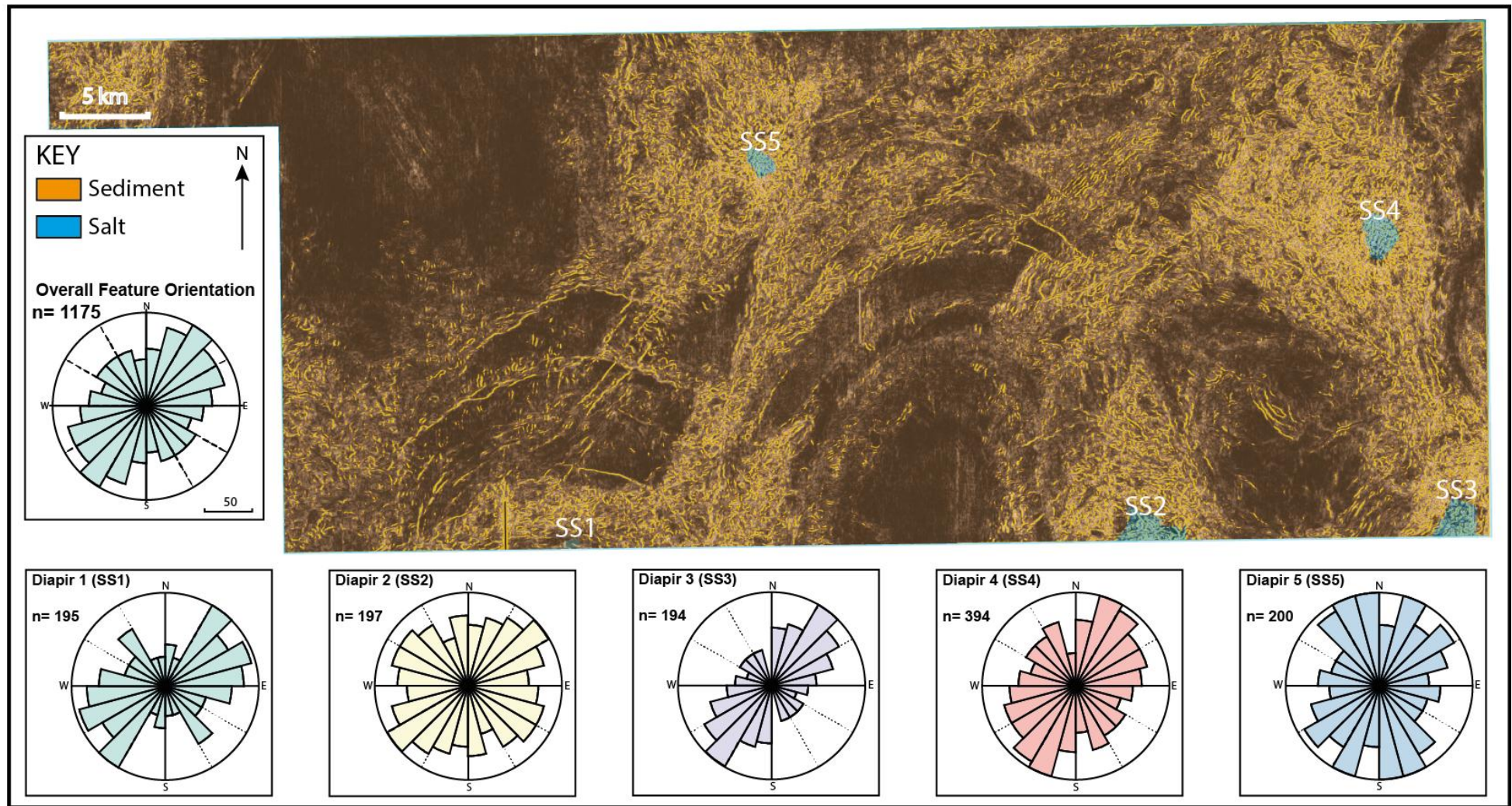


Figure 11: A horizontal time-slice of the Ship Shoal 3D seismic volume at 1272 ms. The time-slice is overlain with the ridge enhancement filter and similarity attribute. Rose diagrams illustrate strike orientations of attribute features within salt diapirs, and surrounding sediment.

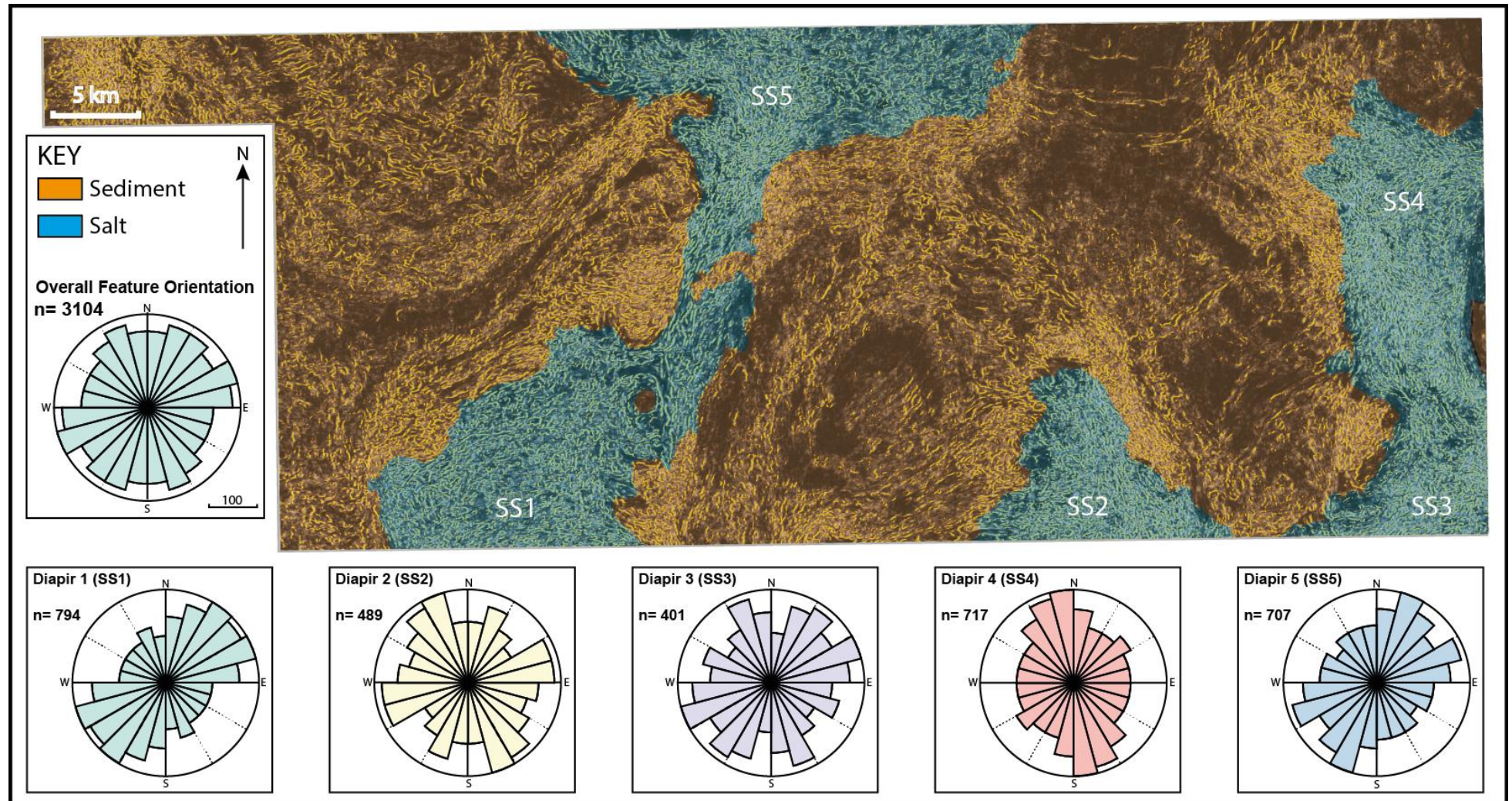


Figure 12: A horizontal time-slice of the Ship Shoal 3D seismic volume at 2800 ms. The time-slice is overlain with the ridge enhancement filter and similarity attribute. Rose diagrams illustrate strike orientations of attribute features within salt diapirs.

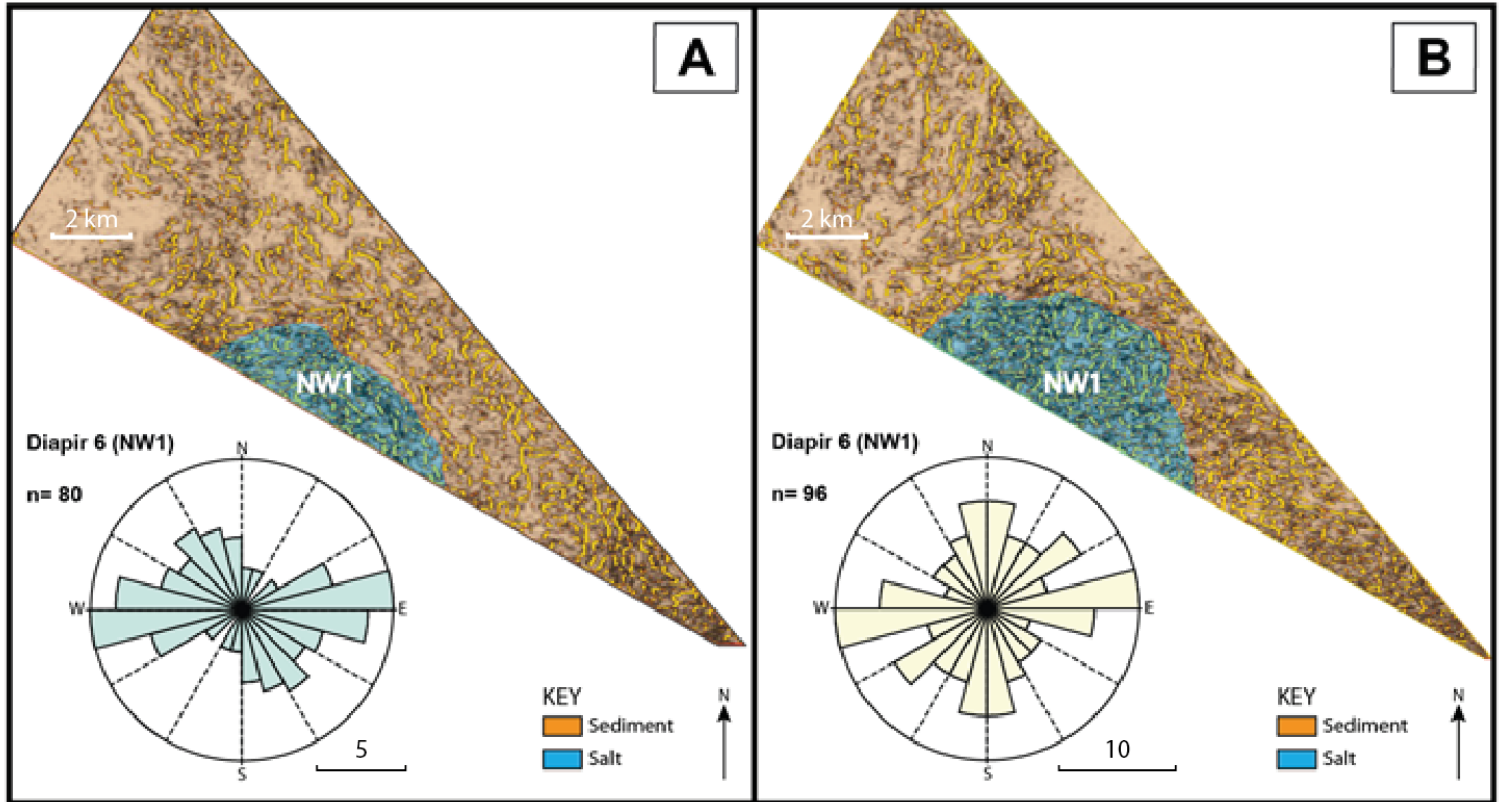


Figure 13: Horizontal time-slices, and rose diagrams of attribute feature strike orientations within salt diapir NW1, from the North-West Gulf Coast 3D seismic volume displaying the ridge enhancement filter and similarity attribute. a) An upper time-slice taken at 2732 ms, and b) A lower time-slice taken at 3824 ms.

5.1 Orientations of Attribute Features

5.1.1 UPPER TIME-SLICES

Rose diagrams displaying strike orientations of attribute features within SS1, SS3 and SS4 strike in a NE-SW direction (Figure 11). Orientations of attribute features within SS2 displayed no predominant strike and were distributed evenly in all directions (Figure 11). Attribute features within SS5 predominantly strike in a N-S direction and the overall strike orientation of diapirs within the Ship Shoal 3D seismic volume was NE-SW (Figure 11). Within the North-West Gulf Coast 3D seismic volume, attribute features within NW1 strike W-E (Figure 13a).

5.1.2 LOWER TIME-SLICES

Attribute features within SS1 and SS5 strike in a NE-SW direction (Figure 12). Features within SS4 strike in a N-S direction (Figure 12). Strike orientations of attribute features within SS2 and SS3 were radially distributed, which was also reflected in the overall strike of diapir attributes (Figure 12). Attribute features within NW1 in the North-West Gulf Coast seismic cube displayed a W-E strike orientation (Figure 13b).

5.2 Densities of Features

Generally, high densities of attribute features occur at the locations of salt diapirs. Within the upper time-slices, attribute feature densities are highest within, and immediately surrounding, the salt diapirs, with low densities observed in the interpreted mini-basins (Figures 11 and 13a). Attribute feature densities within the lower time-slices are highest within the salt diapirs and in a small radius surrounding the salt-sediment interface (Figures 12 and 13b). Attribute densities decrease between adjacent salt diapirs, with the lowest densities observed within the centres of mini-basins (Figures 12 and 13b).

5.3 Geometry of Features

Attribute features occur in the form of thin elongated lines, and vary between linear and curved feature morphologies. Attribute features within salt structures range between 0.5 km and 3 km in length, whereas features within sediments display lengths of less than 1km to 7 km, respectively (Figures 11, 12 and 13).

5.4 Continuity of Features

The attribute features within sediments display higher levels of lateral continuity than in salt. This is observed 5 km north of SS1, where attribute features in the same orientation form 10 km long feature packages running in a W-E direction (Figure 11).

6. DISCUSSION

6.1 Structural Significance of Seismic Attributes

It has been established that 3D seismic attributes can identify structural features over a range of scales, including large-scale faults with displacements of hundreds of metres or more, and small-scale faults with displacements of tens of metres or less (Bahorich and Farmer 1995b, Marfurt et al. 1998a, Chopra and Marfurt 2007a, Francelino and Antunes 2013). Faults observed within the Ship Shoal 3D seismic volume exhibit a strong correlation with large-scale (>2km length) linear features displayed by the ridge enhancement filter and similarity attribute (Figure 14).

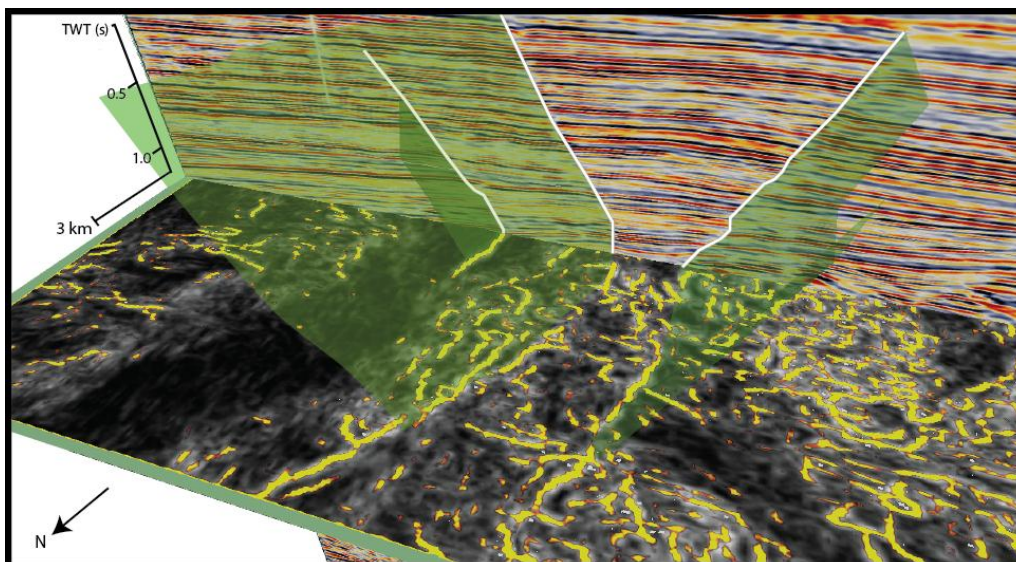


Figure 14: Crossline 3180 crosscutting a time-slice taken at 1272 ms from the Ship Shoal 3D seismic volume. The ridge enhancement filter and similarity attribute has been applied to time slice 1272. Crossline 3180 displays dip-steered amplitudes with mapped faults (white) and mapped fault projections displayed in green.

This correlation implies that attribute features are representative large scale faults within the seismic volume. However, the majority of attribute features within the Ship Shoal and North-West Gulf Coast 3D seismic volumes are of a much smaller scale (1-2 km length), and so cannot be directly related to faults or other geological features in the amplitude display.

6.2 Faults and Fractures: A Power Law Relationship

Previous studies have attempted to form a link between large-scale faults visible on seismic amplitude displays, and sub-seismic amplitude-scale faults and fracture populations (e.g. Walsh et al. 1991, Walsh and Watterson 1992, Yielding et al. 1992). Observations of fault measurements from a variety of scales; regional profiles, seismic mapping, and core from petroleum wells, were taken for comparison (Walsh et al. 1991, Yielding et al. 1992). Results demonstrated a clear alignment between fault characteristics over small (well data), medium (seismic mapping) and large (regional profiles) scales (Walsh et al. 1991, Walsh and Watterson 1992, Yielding et al. 1992). Fault displacement was found to be consistent with a power-law relationship, as the characteristics of faults and fracture populations were found to be comparable over multiple orders of magnitude (Walsh et al. 1991).

If this power-law relationship is true for all fault systems then the regional fault populations within the Gulf of Mexico will share a representative relationship with sub-seismic amplitude scale fractures within the two 3D seismic volumes. NE-SW striking growth faults in the delta top of the Gulf of Mexico DDWFTB accommodate down-dip

extension, and are interpreted to drive regional thin skinned extension within the transitional zone (Figures 1 & 2, Salvador 1987, Marton and Buffler 1999). These NE-SW striking structures are reflected in mapped attribute feature populations within the upper time-slices of both seismic surveys. Overall strike orientations from the attribute features are NE-SW (Figures 11 and 13a); however, attribute features deeper within the salt diapirs do not reflect these strike orientations (Figures 12 and 13b). This suggests that the structural features represented by these attributes behave differently within salt when compared to those in sediment.

6.3 Attribute Features along Lithological Boundaries

As seismic attributes within salt and sediment behave differently, attribute features mapped along the salt-sediment interface are expected to be geometrically different. However, attribute features in both salt and sediment demonstrate analogous behaviours when approaching their lithological interface, with features on both sides running parallel to one another (Figure 15a and 15b).

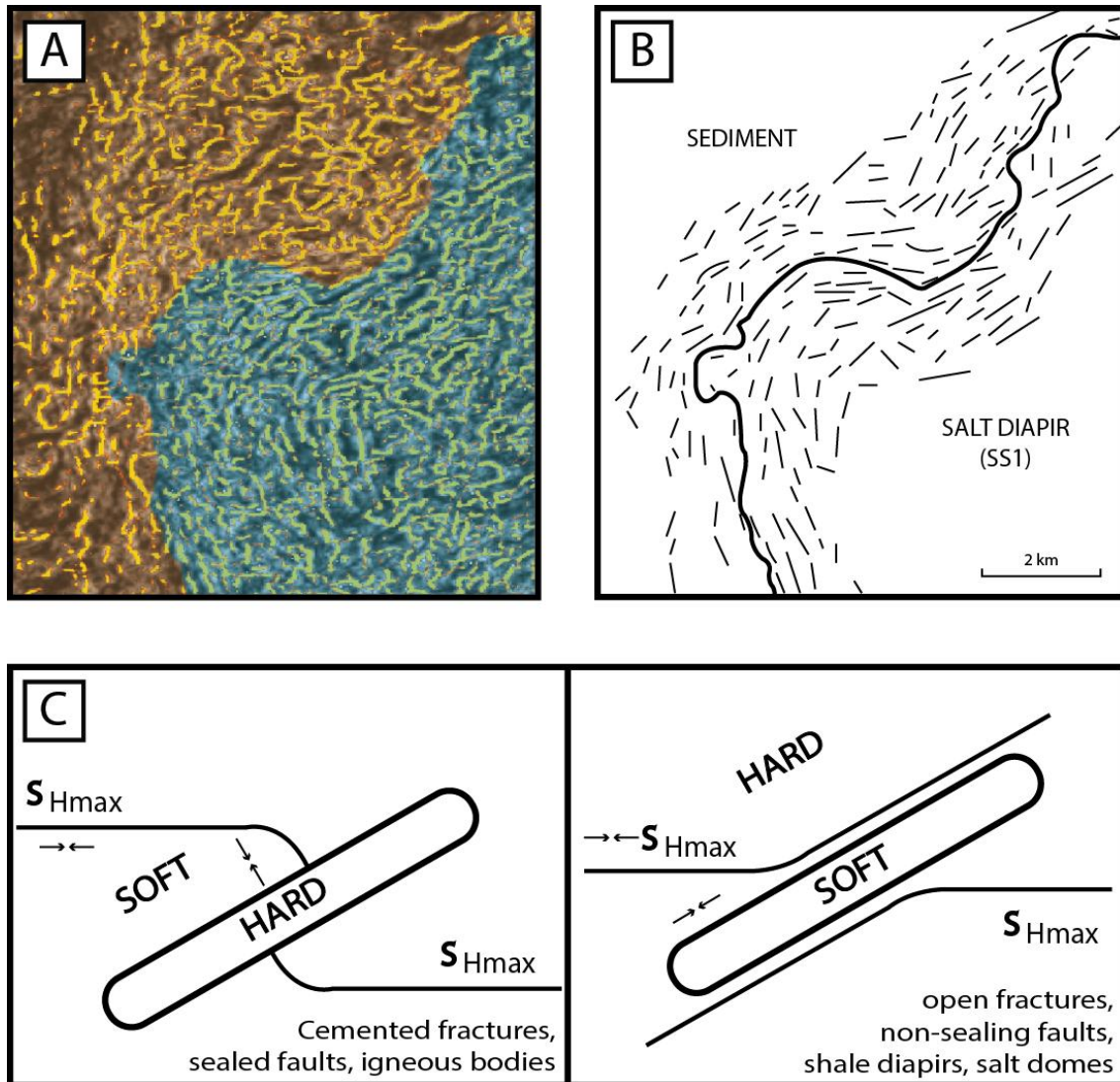


Figure 15: Behaviour of seismic attribute features and maximum horizontal stress (S_{Hmax}) orientations at varying lithological interfaces. a) Ridge enhancement filter and similarity attribute features displayed on a horizontal time-slice at 2800 ms. Attributes representing structural features in salt (blue) and deltaic sediment (orange) form parallel to the salt-sediment interface. b) Simplified schematic interpretation of A highlighting the analogous behaviours between attribute features within salt and deltaic sediment. c) Schematic illustration of S_{Hmax} directions and subsequent deflections when approaching zones of relatively harder or softer rock (Bell 1996).

Similar phenomenon were observed by Bell (1996), where tensile fractures (representing the direction of maximum horizontal stress; S_{Hmax}), were deflected due to contrasts in geomechanical properties in sedimentary rocks. Tensile fractures, when approaching a zone that was relatively harder than the surrounding rock (e.g. an igneous body) were deflected so that the maximum horizontal stress (S_{Hmax}) intersected the

lithological interface at right angles (Figure 15c). Conversely, if the zone was mechanically softer than the surrounding rock (i.e. a salt diapir), stresses were deflected so that S_{Hmax} paralleled the interface (Figure 15c, Bell 1996). Examples of this were observed in the offshore-shore basins of the Scotian Shelf and Grand Banks of Newfoundland, where well data indicated that locally, horizontal stresses are reorientated by as much as 90° (Bell 1989, Adams and Bell 1991). Similar effects have been observed in the North Sea (Teufel and Farrell 1990, Yale et al. 1994) and around the San Andreas Fault (Mount and Suppe 1987). It is accepted that these anomalous orientations were a consequence of structure and the lateral variations in elastic properties of rocks (Ying-Zhen et al. 1994, Bell 1996).

As attribute features, likely to represent natural fractures within the deltaic sediment, are observed to parallel the salt-sediment interface, salt is interpreted to be geomechanically softer than the surrounding sediment. Similar to those within the deltaic sediments, attribute features within salt diapirs; thought to represent natural fractures, form parallel to the salt-sediment interface. However, salt and sediment undergo contrasting deformation styles, raising the question of whether these attribute features continue to represent brittle deformation features, such as natural fractures, in a lithology traditionally associated with ductile deformation (Coward and Stewart 1995, Davison et al. 1996).

In most circumstances, salt detachments undergoing ductile deformation are not expected to form faults and fractures as in the sedimentary overburden. These similar attribute populations may have formed from a later tectonic event, initiating faulting

throughout the inactive detachment. Tectonic driven compression and extension may have triggered collapse or thrusting of extinct salt diapirs, with coeval deformation exhibited within the surrounding sediments.

These events are unlikely to have occurred in the Gulf of Mexico due to the presence of active delta systems fed by the Mississippi River (Figure 1a, Rowan 1997). Active delta systems continue to drive sediment progradation resulting in thin-skinned extension, diapirism and down-dip compression (Wilhelm and Ewing 1972, Rowan 1997). Further observations identify hummocky bathymetry landward of the Sigsbee escarpment, which forms peaks and troughs along the sea floor caused by active salt withdrawal and diapirism (Figure 1b). Diapirism throughout an inactive salt detachment would cease in formation of new and pre-existing salt structures where remaining mini-basins would fill to capacity, producing a planar bathymetry. Therefore, the salt detachment within the Gulf of Mexico is interpreted to be currently active. Attribute features thought to represent natural fractures within the deltaic sediments are also observed within the centres of salt diapirs where strike orientations of attribute feature reflect the same orientations as those towards the flanks (Figures 12 and 13b). Features migrate outwards in rough concentric arrangements, striking parallel to the salt-sediment interface (e.g. Figure 15a and 15b).

6.4 Fractures in Salt

A number of studies have identified morphological relationships between seismic attribute features and structural features (e.g. Bahorich and Farmer 1995b, Marfurt et al. 1998a). Attribute features within salt diapirs exhibit analogous behaviours to tensile fractures in well data (Bell 1996), where strike orientations of attribute features mimic the behaviour of tensile fractures approaching contrasting lithological interfaces (Figure 15). Further relationships were observed by Bailey et al. (2014), where attribute features displayed similar strike orientations to natural fractures identified in well image logs. These observations reinforce the conclusion that attributes are, in fact, representative of structural fabrics and not merely noise within a seismic 3D volume.

Fractures observed in sediments within the upper crust are expected to form due to brittle failure. However, ductile shear is well documented to dominate salt tectonics (Urai et al. 1986, Morley and Guerin 1996, Rowan et al. 2004, Fossen 2010). Purely ductile or plastic deformation of salt is expected to produce folding by Poiseuille and Couette flow (Figures 3a and 3b, Jaeger and Neville 1979, Fossen 2010). Deformation of salt by Poiseuille flow can result in antiformal fold structures due to the restriction of flow against the salt-sediment interface (Jaeger and Neville 1979). Ridge enhancement filter and similarity attributes may characterise high angle isoclinal folds throughout the limbs of antiforms, or ductile shear between salt layers. Similarly, high angle folds may occur from Couette flow, where attribute features represent high angle folds formed from simple shearing between salt layers (Jaeger and Neville 1979, Davison et al. 1996).

However, in cases of high strain rates, ductile salt can produce brittle faulting (Davison et al. 1996, Vendeville and Jackson 1992b). Faulting is interpreted to have formed during early diapirism, as salt diapirs are initiated in the brittle regime at depths shallower than the brittle-ductile transition (Vendeville and Jackson 1992b). Diapirism induced faulting is likely to propagate into the sedimentary overburden, forming brittle offsets such as those visible along the western flank of SS3 (Figure 6c). Attribute features displayed within the Ship Shoal and North-West Gulf Coast 3D seismic volumes are inferred to represent brittle faults, rather than ductile folds. Ridge enhancement filter and similarity attribute features associated with visible faults, within a dip-steered seismic section, are of identical geometry to adjacent sub-kilometre attribute features (Figure 14). Additionally, attribute features show little to no representation of broad synclinal folds representative of mini-basins (Figure 11).

Evidence for brittle deformation of salt implies that attribute features within salt diapirs may represent sub-seismic amplitude scale faults and fractures. The high densities of attribute features form a systematic arrangement within the diapirs, where faults and fractures appear parallel to the salt-sediment interface. Deformation is interpreted to be coeval with diapirism, and is facilitated by Poiseuille and Couette flow mechanics. During reactive and active diapirism, buoyant mobilisation of salt facilitates brittle shear between salt layers (Davison et al. 1996). Shearing by means of Poiseuille flow would produce a series of thrust faults forming parallel to salt-sediment interface, analogous to flexing a deck of cards. Additional deformation by Couette flow is inferred to produce simple shearing of salt layers, where buoyancy towards the centre of the diapir generates a series of normal faults paralleling the diapirs flanks. The antiformal

nature of diapir growth is expected to produce outwards dipping shear, forming the concentric patterns displayed by attribute features (Figures 11, 12 and 13). Determining which mode of deformation takes place throughout a diapir is difficult to identify, as shear sense cannot be established from the time-slice attribute maps.

While a single structural mode of deformation is plausible, deformation of the salt detachment is likely a combination of both brittle and ductile mechanisms. Salt is intrinsically weak, exhibiting low compressive strength with the ability to flow plastically at low shear stresses (Davis and Engelder 1985, Davison et al. 1996, Bell 2006). The elastic properties of salt are defined by Young's modulus, wherein salt is represented as mechanically soft (Urai et al. 1986). Deformation of salt during diapir growth is known to exhibit high strain rates (Schoenherr et al. 2010), and is interpreted to display a multi-layer Poiseuille and Couette velocity profile (Figure 3d, Davison et al. 1996). Similar to Davidson (1996), flow of viscous salt in a confined layer exhibits a Poiseuille velocity profile, with the highest flow velocity in the centre of the layer. Interbedded resistive layers (i.e. carbonates) within the evaporite sequence produce increased drag, and form the bounding edges of the salt (Figure 3A, Schoenherr et al. 2010). Furthermore, resistive sequences facilitate subsequent Couette flow, where the velocity of advancing salt is dependent on the relative resistance along its bounding edges (Figure 3c).

However, once the elastic limit of salt is exceeded, brittle mode deformation is expected to dominate, where faults and fractures form along a resistive bounding layer. During diapir formation, the sedimentary overburden forms a highly resistive bounding edge,

generating an increasing gradient of flow velocities deeper into the salt. Buoyant uplift of salt layers is therefore interpreted to produce an arrangement of outward dipping normal faults, striking parallel to the salt-sediment interface.

This style of deformation provides a viable explanation for the high densities of attribute features observed within salt diapirs, as brittle failure is observed on a sub-kilometre scale (Figures 11, 12 and 13). Additionally, strike orientations of diapir related normal faults are consistent with the orientations of seismic attribute features within mapped salt diapirs, making it likely that attribute features continue to represent natural faults and fractures, and that these form a coherent structural fabric within the salt.

7. CONCLUSIONS

The purpose of this study was to identify deformation occurring in the salt detachment within the Gulf of Mexico using seismic attribute analysis applied to two 3D seismic volumes. Seismic interpretation identified six diapirs from the Gulf of Mexico (Figure 10). It is evident that diapirs SS1 and NW1 have undergone reactive diapirism, with subsequent interpretation classifying diapirs SS2, SS3, SS4 and SS5 as active.

Seismic attribute analysis involved applying the ridge enhancement filter and similarity attributes to four horizontal time-slices (Figures 11, 12 and 13). Interpretation of seismic attribute features identified contrasting behaviours between attribute feature populations within salt diapirs and the overlying deltaic sediments. Attribute feature

orientations within deltaic sediments reflect NE-SW striking growth faults present within the delta top, whereas those within the underlying salt diapirs display no predominant orientation. It is interpreted that the lack of a dominant strike orientation within the salt diapirs is due to the radially concentric nature of the attribute features.

Attribute features display a clear alignment with kilometre scale faults visible in seismic section (Figure 14). Additionally, sub-kilometre length attribute features display comparable behaviours to those of tensile fractures when approaching a geomechanically contrasting interface (Figure 15). Therefore, the ridge enhancement filter and similarity attribute features are consistent with a power-law relationship, and are accepted to be representative of faults and fractures over a range of magnitudes.

Current consensus of salt deformation within an active detachment is wholly ductile; however, attribute features observed within salt diapirs suggests that both brittle and ductile deformation is occurring. Active salt detachments within the Gulf of Mexico produce high strain rates during diapirism, where multi-layer Poiseuille and Couette flow mechanics drive ductile deformation. Once the elastic limit of salt is exceeded, brittle mode deformation is expected to dominate, where faults and fractures form along resistive bounding layers.

ACKNOWLEDGMENTS

Rosalind King

Adam Bailey

Alex Robson

Lachlan Richards

David Kulikowski

Ernest Swierczek

Ian West

Sam White

Alexandra Carter

Katie Howard

ASP

REFERENCES

- ADAMS J. & BELL J. S. 1991 Crustal stresses in Canada. In SIEMMONS D. B., *et al.* eds. Neotectonics of North America. Boulder, Colorado: Geological Society of America.
- ALSOP G. I. 1996 Physical modelling of fold and fracture geometries associated with salt diapirism, *Geological Society, London, Special Publications*, vol. 100, no. 1, pp. 227-241.
- BACK S., *et al.* 2008 Three-dimensional restoration of original sedimentary geometries in deformed basin fill, onshore Brunei Darussalam, NW Borneo, *Basin Research*, vol. 20, no. 1, pp. 99-117.
- BACKÉ G., *et al.* 2012 Seismic Attribute and Structural Interpretation - It Take Two To Tango... *APPEA Journal*, pp. 437-454.
- BAHORICH M. & FARMER S. 1995a 3-D seismic discontinuity for faults and stratigraphic features: The coherence cube, *The Leading Edge*, vol. 14, no. 10, pp. 1053-1058.
- 1995b 3-D seismic discontinuity for faults and stratigraphic features: The coherence cube, *The Leading Edge*, vol. 14, no. 10, pp. 1053-1058.
- BAHROUDI A. & KOYI H. 2003 Effect of spatial distribution of Hormuz salt on deformation style in the Zagros fold and thrust belt: an analogue modelling approach, *Journal of the Geological Society*, vol. 160, no. 5, pp. 719-733.
- BAILEY A., *et al.* 2014 Remote sensing of subsurface fractures in the Otway Basin, South Australia, *Journal of Geophysical Research: Solid Earth*, vol. 119, pp. 10-20.
- BELL F. G. 2006 Engineering Geology. Butterworth-Heinemann, GBR.
- BELL J. S. 1989 Case studies in Canadian petroleum geology; Vertical migration of hydrocarbons at Alma, offshore Eastern Canada, *Bulletin of Canadian Petroleum Geology*, vol. 37, no. 3, pp. 358-364.
- 1996 In Situ Stresses in Sedimentary Rocks (Part 2): Applications of Stress Measurements, *Journal of the Geological Association of Canada*, vol. 23, no. 3, pp. 135-153.
- BERTHELOT A., SOLBERG A. H. S. & GELIUS L.-J. 2013 Texture attributes for detection of salt, *Journal of Applied Geophysics*, vol. 88, no. 0, pp. 52-69.
- BIRD D. E., *et al.* 2005 Gulf of Mexico tectonic history: Hotspot tracks, crustal boundaries, and early salt distribution, *AAPG Bulletin*, vol. 89, no. 3, pp. 311-328.
- BOUMA A. & ROBERTS H. 1990 Northern Gulf of Mexico continental slope, *Geo-Marine Letters*, vol. 10, no. 4, pp. 177-181.
- BRUN J.-P., SOKOUTIS D. & VAN DEN DRIESSCHE J. 1994 Analogue modeling of detachment fault systems and core complexes, *Geology*, vol. 22, no. 4, pp. 319-322.
- CHEHRAZI A., RAHIMPOUR-BONAB H. & REZAAE M. R. 2013 Seismic data conditioning and neural network-based attribute selection for enhanced fault detection, *Petroleum Geoscience*, vol. 19, no. 2, pp. 169-183.
- CHOPRA S. & MARFURT K. 2007a Curvature attribute applications to 3D surface seismic data, *The Leading Edge*, vol. 26, no. 4, pp. 404-414.
- 2007b Lateral Changes in Amplitude and Pattern Recognition. Seismic Attributes for Prospect Identification and Reservoir Characterization. pp. 99-122. Society of

- Exploration Geophysicists and European Association of Geoscientists and Engineers.
- CHOPRA S. & MARFURT K. J. 2005 Seismic attributes — A historical perspective, *Geophysics*, vol. 70, no. 5, pp. 3SO-28SO.
- 2007c Volumetric curvature attributes add value to 3D seismic data interpretation, *The Leading Edge*, vol. 26, no. 7, pp. 856-867.
- COHEN H. A. & MCCLAY K. 1996 Sedimentation and shale tectonics of the northwestern Niger Delta front, *Marine and Petroleum Geology*, vol. 13, no. 3, pp. 313-328.
- COWARD M. & STEWART S. 1995 Salt-Influenced Structures in the Mesozoic–Tertiary Cover of the Southern North Sea, U.K., *AAPG Memoir*, vol. 65, pp. 229-250.
- CRUTCHLEY G. J., *et al.* 2011 Insights into active deformation in the Gulf of Cadiz from new 3-D seismic and high-resolution bathymetry data, *Geochemistry, Geophysics, Geosystems*, vol. 12, no. 7, p. Q07016.
- DAVIS D. M. & ENGELDER T. 1985 The role of salt in fold-and-thrust belts, *Tectonophysics*, vol. 119, no. 1–4, pp. 67-88.
- DAVISON I., ALSOP I. & BLUNDELL D. 1996 Salt tectonics: some aspects of deformation mechanics, *Geological Society, London, Special Publications*, vol. 100, no. 1, pp. 1-10.
- DE ROOIJ M. & TINGDAHL K. 2002 Meta-attributes—the key to multivolume, multiattribute interpretation, *The Leading Edge*, vol. 21, no. 10, pp. 1050-1053.
- DOOLEY T. P., JACKSON M. P. A. & HUDEC M. R. 2007 Initiation and growth of salt-based thrust belts on passive margins: results from physical models, *Basin Research*, vol. 19, no. 1, pp. 165-177.
- FOSSEN H. 2010 Structural Geology. Cambridge University, New York, United States of America.
- FRANCELINO A. V. M. & ANTUNES A. F. 2013 Applying Filters and Seismic Attributes for Enhancing Faults in the 3D Seismic Survey of Alto De Siririzinho (Sergipe-Alagoas Basin, Northeast Brazil), *Revista Brasileira de Geofísica*, vol. 31, no. 1, pp. 109-123.
- GALLOWAY W. E. 2008 Chapter 15 Depositional Evolution of the Gulf of Mexico Sedimentary Basin. In ANDREW D. M. ed. *Sedimentary Basins of the World*. pp. 505-549. Elsevier.
- GALLOWAY W. E., *et al.* 2000 Cenozoic Depositional History of the Gulf of Mexico Basin, *AAPG Bulletin*, vol. 84, no. 11, pp. 1743-1774.
- HANSBERRY R., *et al.* 2014 Detachments in Shale: Controlling Characteristics on Fold-Thrust Belt Style, *EGU General Assembly*.
- HESTHAMMER J. & FOSSEN H. 1997 Seismic attribute analysis in structural interpretation of the Gullfaks Field, northern North Sea, *Petroleum Geoscience*, vol. 3, no. 1, pp. 13-26.
- HUDEC M. R., JACKSON M. P. A. & PEEL F. J. 2013a Influence of deep Louann structure on the evolution of the northern Gulf of Mexico, *AAPG Bulletin*, vol. 97, no. 10, pp. 1711-1735.
- HUDEC M. R., *et al.* 2013b Jurassic evolution of the Gulf of Mexico salt basin, *AAPG Bulletin*, vol. 97, no. 10, pp. 1683-1710.
- IACOPINI D. & BUTLER R. W. H. 2011 Imaging deformation in submarine thrust belts using seismic attributes, *Earth and Planetary Science Letters*, vol. 302, no. 3–4, pp. 414-422.

- JACKSON M. P. A. & SENI S. J. 1983 Geometry and evolution of salt structures in a marginal rift basin of the Gulf of Mexico, east Texas, *Geology*, vol. 11, no. 3, pp. 131-135.
- JACKSON M. P. A. & TALBOT C. J. 1986 External shapes, strain rates, and dynamics of salt structures, *Geological Society of America Bulletin*, vol. 97, no. 3, pp. 305-323.
- JACKSON M. P. A., VENDEVILLE B. C. & SCHULTZ-ELA D. D. 1994 Salt-related structures in the Gulf of Mexico; a field guide for geophysicists, *The Leading Edge*, vol. 13, no. 8, pp. 837-842.
- JAEGER J. C. & NEVILLE G. W. 1979 *Fundamentals of Rock Mechanics*. (3rd edition). Chapman and Hall.
- KING R. C. & BACKÉ G. 2010 A balanced 2D structural model of the Hammerhead Delta–Deepwater Fold-Thrust Belt, Bight Basin, Australia, *Australian Journal of Earth Sciences*, vol. 57, no. 7, pp. 1005-1012.
- KING R. C., *et al.* 2009 Present-day stress and neotectonic provinces of the Baram Delta and deep-water fold–thrust belt, *Journal of the Geological Society*, vol. 166, no. 2, pp. 197-200.
- KRÉZSEK C., ADAM J. & GRUJIC D. 2007 Mechanics of fault and expulsion rollover systems developed on passive margins detached on salt: insights from analogue modelling and optical strain monitoring, *Geological Society, London, Special Publications*, vol. 292, no. 1, pp. 103-121.
- MARFURT K., *et al.* 1998a 3-D seismic attributes using a semblance-based coherency algorithm, *GEOPHYSICS*, vol. 63, no. 4, pp. 1150-1165.
- MARFURT K. J., *et al.* 1998b Suppression of the acquisition footprint for seismic sequence attribute mapping, *Geophysics*, vol. 63, no. 3, pp. 1024-1035.
- MARSH N. A. 2008 The influences of crustal extension, salt tectonics and gravity-driven deformation on the structural evolution of the Halten Terrace, offshore mid-Norway: new insights from 3D seismic data and fault analysis, *Durham theses, Durham University*, pp. 23-196.
- MARTIN R. G. 1978 Northern and eastern Gulf of Mexico continental margin: Stratigraphic and structural framework, *AAPG Studies in Geology*, vol. 7, pp. 21-42.
- MARTON G. L. & BUFFLER R. T. 1999 Chapter 3 Jurassic—early cretaceous tectono-paleogeographic evolution of the southeastern gulf of Mexico basin. In MANN P. ed. *Sedimentary Basins of the World*. pp. 63-91. Elsevier.
- MCCLAY K., DOOLEY T. & ZAMORA G. 2003 Analogue models of delta systems above ductile substrates, *Geological Society, London, Special Publications*, vol. 216, no. 1, pp. 411-428.
- MORLEY C. K. & GUERIN G. 1996 Comparison of gravity-driven deformation styles and behavior associated with mobile shales and salt, *Tectonics*, vol. 15, no. 6, pp. 1154-1170.
- MORLEY C. K., *et al.* 2011 Deepwater fold and thrust belt classification, tectonics, structure and hydrocarbon prospectivity: A review, *Earth-Science Reviews*, vol. 104, no. 1–3, pp. 41-91.
- MOUNT V. S. & SUPPE J. 1987 State of stress near the San Andreas fault: Implications for wrench tectonics, *Geology*, vol. 15, no. 12, pp. 1143-1146.

- MOURGUES R. & COBBOLD P. R. 2006 Sandbox experiments on gravitational spreading and gliding in the presence of fluid overpressures, *Journal of Structural Geology*, vol. 28, no. 5, pp. 887-901.
- NUNN J. A. 1984 Subsidence histories for the Jurassic sediments of the northern Gulf Coast: Thermal-mechanical model. In VENTRESS W. P. S., *et al.* eds. Proceedings of the 3rd Annual Gulf Coast Section SEPM Foundation Research Conference. pp. 309-322.
- RATCLIFF D., GRAY S. & WHITMORE N. 1992 Seismic imaging of salt structures in the Gulf of Mexico, *The Leading Edge*, vol. 11, no. 4, pp. 15-31.
- ROBERTS A. 2001 Curvature attributes and their application to 3D interpreted horizons, *First Break*, vol. 19, no. 2, pp. 85-100.
- ROWAN M. G. 1997 Three-dimensional geometry and evolution of a segmented detachment fold, Mississippi Fan foldbelt, Gulf of Mexico, *Journal of Structural Geology*, vol. 19, no. 3-4, pp. 463-480.
- ROWAN M. G., PEEL F. J. & VENDEVILLE B. C. 2004 Gravity-driven Fold Belts on Passive Margins, in K. R. McClay, ed, Thrust tectonics and hydrocarbon systems:, *AAPG Memoir*, vol. 82, pp. 157-182.
- ROWAN M. G. & VENDEVILLE B. C. 2006 Foldbelts with early salt withdrawal and diapirism: Physical model and examples from the northern Gulf of Mexico and the Flinders Ranges, Australia, *Marine and Petroleum Geology*, vol. 23, no. 9-10, pp. 871-891.
- SALVADOR A. 1987 Late Triassic-Jurassic paleogeography and origin of Gulf of Mexico Basin, *AAPG Bulletin*, vol. 71, no. 4, pp. 419-451.
- SAVA P. & BIONDI B. 2004 Wave-equation migration velocity analysis. II. Subsalt imaging examples, *Geophysical Prospecting*, vol. 52, no. 6, pp. 607-623.
- SAWYER D. S., BUFFER R. T. & PILGER JR R. H. 1991 The crust under the Gulf of Mexico, A. Salvador, ed, *The Gulf of Mexico basin: Geological Society of America, Decade of North American Geology*, vol. J, pp. 53-72.
- SCHOENHERR J., *et al.* 2010 Deformation mechanisms of deeply buried and surface-piercing Late Pre-Cambrian to Early Cambrian Ara Salt from interior Oman, *International Journal of Earth Sciences*, vol. 99, no. 5, pp. 1007-1025.
- STEWART R. R. 1985 Median Filtering: Review and a New F/K Analogue Design, *Journal of the Canadian Society of Exploration Geophysicists*, vol. 21, no. 1, pp. 54-63.
- TEUFEL L. W. & FARRELL H. E. 1990 In-situ stress and natural fracture distribution in the Ekofisk Field, North Sea. North Sea Chalk Symposium. pp. 1-33. Copenhagen.
- TINGDAHL K. M., BRIL A. H. & DE GROOT P. F. 2001 Improving seismic chimney detection using directional attributes, *Journal of Petroleum Science and Engineering*, vol. 29, no. 3-4, pp. 205-211.
- TREVIÑO R. H. & VENDEVILLE B. C. 2008 Origin of coast-perpendicular extensional faults, western Gulf of Mexico: The relationship between an early-stage ridge and a late-stage fault, *AAPG Bulletin*, vol. 92, no. 7, pp. 951-964.
- TRUDGILL B. D., *et al.* 1999 The Perdido Fold Belt, Northwestern Deep Gulf of Mexico, Part 1: Structural Geometry, Evolution and Regional Implications1, *AAPG Bulletin*, vol. 83, no. 1, pp. 88-113.
- URAI J. L., *et al.* 1986 Weakening of rock salt by water during long-term creep, *Nature*, vol. 324, no. 6097, pp. 554-557.

- VENDEVILLE B. C. & JACKSON M. P. A. 1992a The fall of diapirs during thin-skinned extension, *Marine and Petroleum Geology*, vol. 9, no. 4, pp. 354-371.
- 1992b The rise of diapirs during thin-skinned extension, *Marine and Petroleum Geology*, vol. 9, no. 4, pp. 331-354.
- WALSH J., WATTERSON J. & YIELDING G. 1991 The importance of small-scale faulting in regional extension, *Nature*, vol. 351, no. 6325, pp. 391-393.
- WALSH J. J. & WATTERSON J. 1992 Populations of faults and fault displacements and their effects on estimates of fault-related regional extension, *Journal of Structural Geology*, vol. 14, no. 6, pp. 701-712.
- WARREN J. K. 2006 *Evaporites: Sediments, Resources and Hydrocarbons: Sediments, Resources, and Hydrocarbons*. Springer.
- WEIMER P. & DAVIS T. L. 1996 *Applications of 3-D Seismic Data to Exploration and Production*. American Association of Petroleum Geologists.
- WILHELM O. & EWING M. 1972 Geology and History of the Gulf of Mexico, *Geological Society of America Bulletin*, vol. 83, no. 3, pp. 575-600.
- WU S., BALLY A. W. & CRAMEZ C. 1990 Allochthonous salt, structure and stratigraphy of the north-eastern Gulf of Mexico. Part II: Structure, *Marine and Petroleum Geology*, vol. 7, no. 4, pp. 334-370.
- YALE D. P., *et al.* In-situ stress orientation and the effects of local structure - Scott Field, North Sea. Society of Petroleum Engineers.
- YASSIR N. A. & ZERWER A. 1997 Stress regimes in the Gulf Coast, offshore Louisiana; data from well-bore breakout analysis, *AAPG Bulletin*, vol. 81, no. 2, pp. 293-307.
- YIELDING G., WALSH J. & WATTERSON J. 1992 The prediction of small-scale faulting in reservoirs, *First Break*, vol. 10, pp. 449-449.
- YING-ZHEN Z., DUSSEAU M. B. & YASSIR N. A. 1994 Effects of rock anisotropy and heterogeneity on stress distributions at selected sites in North America, *Engineering Geology*, vol. 37, no. 3-4, pp. 181-197.

APPENDIX A: METHODOLOGY

Step 1: Initial set-up of seismic data and exporting it into a SEG-Y file using

Kingdom

1. Open Kingdom and select the “*Open Project...*” option. Select either the ShipShoal_Area 1 or NorthWest_GC .tks files and click “*Open*”.
2. Select “*No*” in the *Migrate Project Database* window to continue loading the project.
3. When the *Colour Path Not Found* window appears, select “*OK*” to continue.
4. In the *Project Tree*, scroll down until you locate the ShipShoal_Area1 or NorthWest_GC data under the Surveys/All Surveys folder, right click and select “*Export > SEG Y...*”.
5. The *Export SEG Y* window will appear with detailed information of the data. Take note of the *Inline* and *Trace Number Starts in Byte* and press “*OK*”.
6. Select a folder where the SEG Y (.sgy) file is to be saved and click “*Save*”.

The following steps are sourced from the dGB Earth Sciences – OpendTect version 4.6 “*Introduction to OpendTect*” Training Manual - January 2014. The manual is free to download from

<http://www.opendtect.org/index.php/support/tutorials/training>.

Step 2: Setup Survey and Load SEG-Y Data (pp. 205-206 of training manual)

1. Open OpendTect and select the “*Select/Setup...*” option under the *Survey* menu.

2. Before creating a new survey, firstly we must select a set data root where all our seismic data will be saved. Select “*Set Data Root...*” and select the folder where your seismic data stored.
3. Select the “*New*” option to set up a new survey.
4. In the next window, name the new survey *Ship_Shoal_Area_1* or *NW_GC* and select the *Survey type* from the drop down menu (in this case select “*Only 3D*”). Select “*Scan SEG-Y file(s)...*” from *Define by*, and specify the *Domain* as “*Time*”. Select “*Ok*” to continue.
5. Select the Input SEG-Y file (F:\Honours 2014\GOM Data\Seismic Data\NW Gulf Coast\NW_GC.sgy).
6. Leave the remaining as default and select “*Next*”.
7. In the *SEG-Y Scan* window under the *Locations* tab input 17 and 25 into the *In-line byte* and *Cross-line byte* fields respectively. Leave the remaining tab fields as default, and select the optional output names *Ship_Shoal_Area_1* or *NW_GC* and select “*Go*”.
8. The original *Survey setup* window will appear with the completed *Survey ranges*. Select “*Dismiss*” and click “*Ok*” to complete the survey setup. Select the new survey and click “*OK (Select)*” and *OpendTect* will prompt you to load the seismic file that has just been scanned. Click “*Yes*”, and specify the *Output Cube* file names (*Ship_Shoal_Area_1* or *NW_GC*) and press “*Go*” to load the seismic data in *OpendTect*. On import completion, you will see an information window giving some details of the cube. Click “*Ok*” to dismiss this, once read.

9. Finally, load an inline (refer to pp. 22 of training manual) to check the data. For both surveys you will need to change the vertical scale. To do this, go to “*View*” and adjust the *Z-scale* to 10 for both cubes.

The data as it exists contains moderate levels of noise and poor lateral continuities. To amend these issues we are going to apply a Dip-Steered Median Filter to the two 3D cubes, which outputs a median value of the input amplitudes at a given point, essentially “smoothing” continuous amplitudinal continuities. Dip-Steered Median Filters require three components; the original seismic data (i.e. *Ship_Shoal_Area_1/ NW_GC*), a Detailed SteeringCube, and a Background SteeringCube.

Step 3: Creating a Detailed SteeringCube Computation (pp. 82)

1. Bring up the *Create Steering Seismics* window via *Processing > Dip Steering > Create*.
2. Select the *Ship_Shoal_Area_1 or NW_GC* seismics as the input and the *BG fast steering* as Steering algorithm.
3. Use the default *Calculation stepout* 1, 1, 1. Leave *Specify maximum dip* as *No* (default).
4. Leave the default *Filter result* as *Median* and select a *Filter stepout* of 1, 1, 3.
5. Give the SteeringCube a name (e.g *BG111_MF113*) and click “*Proceed*”.

Step 4: Creating a Background SteeringCube Computation (pp. 88)

1. Bring up the *Create Steering Seismics* window via *Processing > Dip Steering > 3D > Filter...*
2. In the *Input Steering Data* drop down menu, select the *Detailed SteeringCube (BG111_MF113)*.
3. Use the default *Filter type* and input a *Filter stepout* of *inl:5/crl:5/sample:0*.
4. Give the *SteeringCube* a name (e.g. *Background SC*), and select “*Proceed*” to compute (this can take up to a day on fast computers).

Step 5: Creating a Dip-Steered Median Filter (pp. 89-91)

1. Before we apply the filter to the data we need to define an attribute of type “Volume statistics”. Under the *Analysis* tab select *Attributes*. This will open up the *Attribute Set 3D* window.
2. In the first drop down menu select *Statistics* followed by *Volume Statistics* in its adjacent counterpart.
 - Input Data: *Ship_Shoal_Area_1* or *NW_GC*
 - Time gate (ms): [0,0]
 - Shape: *Cylinder*
 - Stepout: *inl:1/crl:1*
 - Min nr of valid traces: 1
 - Output statistics: *Median*
 - Steering: *Full > Background SC*
3. Use the *Evaluate attribute* tool to evaluate the step-out: initial value 0-0, increment 1-1, and 5 slices.

4. Name the attribute “*DSMF*” and “*Add as new*”, followed by “*Ok*” to complete.

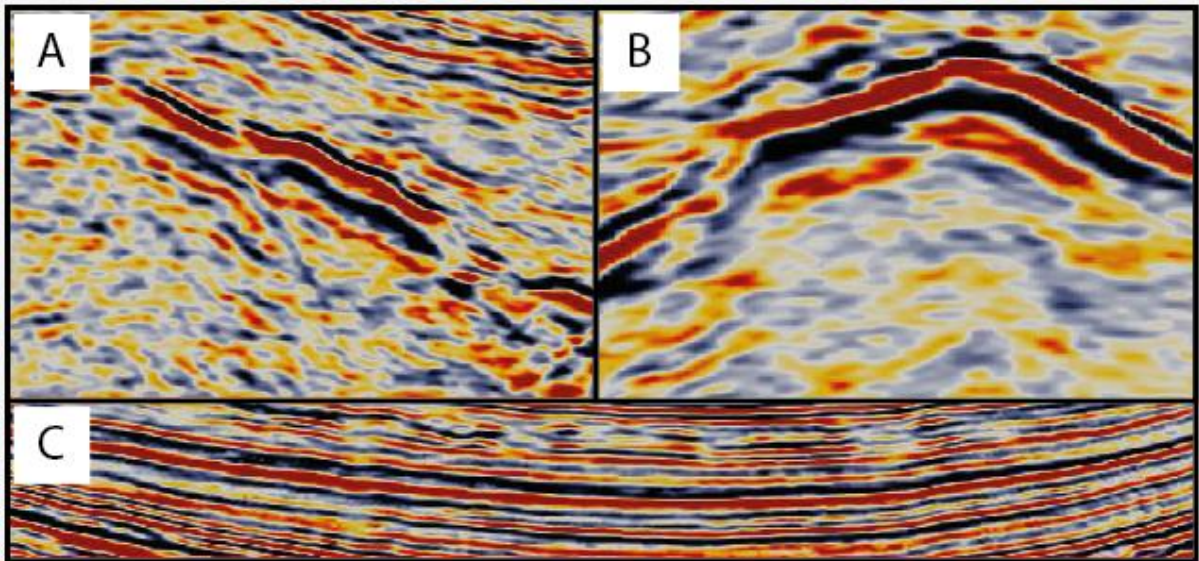
Step 6: Horizon Tracking and Interpretation (pp. 61-66)

In this study we will be tracking a top salt horizon in both cubes, followed by an upper sediment horizon, in order to gain an understanding of the evolution of each diapir. Our approach to tracking the horizons is to form a grid of inlines and crosslines to maximise accuracy, whilst being effective in our coverage of each horizon.

1. Add an inline using the attribute Dip-Steered Median Filter (DSMF).
2. Right-click *Horizon* in the tree and select *New...* This will launch a window with the following tabs: Mode, Event, Similarity, Properties. These settings will have to be reset at the beginning of each new session.
3. Mode:
 - Select *Tracking in Volume*.
4. Event:
 - Select the *Input data DSMF*.
 - From the *Event type* drop down select *Min* (if picking a negative horizon) or *Max* (if picking a positive horizon).
 - *Leave remaining fields as default*.
5. Similarity:
 - Leave as default (No)
6. Properties:
 - Leave *Horizon colour* and *seed colour/ size* as default.
7. DipSteer:
 - Leave as default (No).

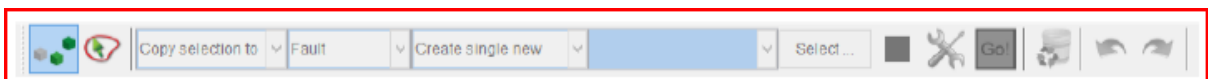
An effectively picking a horizon will involve tracking along a strong reflector that is persistent throughout much of the cube. A good technique is to find patterns or trends in the data that allow you to identify the horizon, as depicted in Figure 1. The top salt reflectors are easily identifiable as they follow diapirism throughout the cube.



Figure 1: a & b) A top salt package consisting of a strong negative (red) reflector adjacent to a strong positive (blue) reflector, which is underlain by a weak, disseminated negative reflector (Crossline 2300, Ship Shoal 3D cube. c) Strong and persistent shallow sedimentary reflectors (Crossline 2300, Ship Shoal 3D cube).



Step 7: Picking and Interpreting Faults (pp. 68-71)

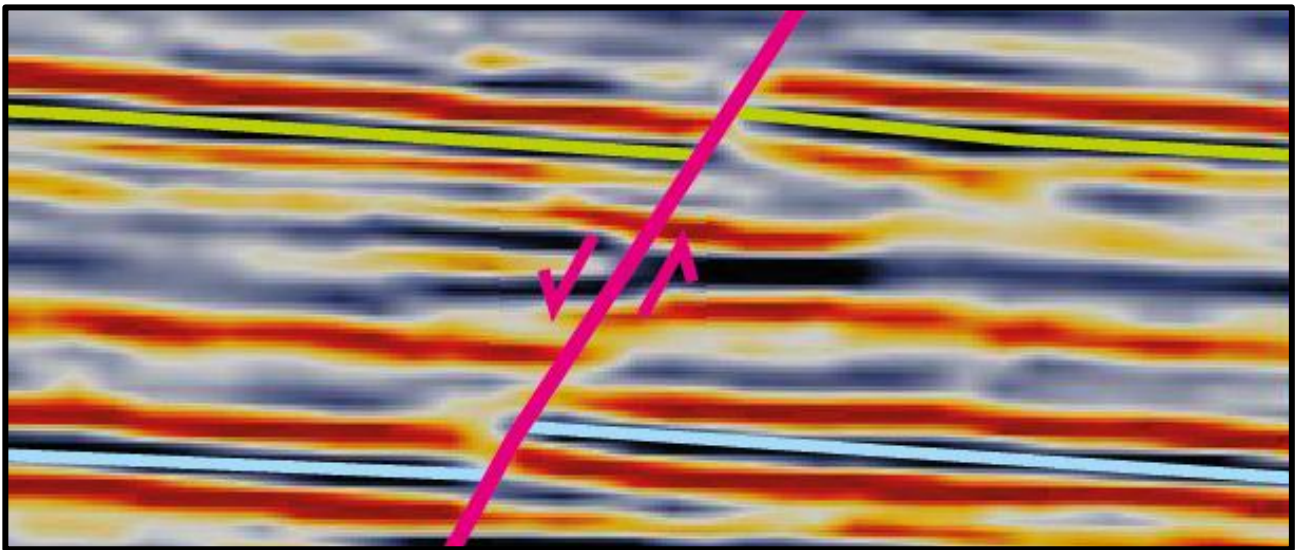
1. Right click “*FaultStickSet*” in the tree, select *New...*
2. The fault interpretation toolbar at the bottom becomes active; the *edit stick* button is selected by default.



- Pick faults in any order of preference (from top to bottom, middle etc.) by clicking on the seismic section.
 - After picking fault sticks, stick nodes can be *dragged* by holding down the left mouse button over a node and dragging it to a new location.
 - Individual stick nodes can be removed with Ctrl + left mouse click.
 - Multiple fault sticks can be removed by selecting the polygon tool  and selecting one or more seeds. The stick nodes change colour (to green) when selected and the polygon will disappear.
 - Thereafter immediately click the recycle icon . Deselection of specific sticks within the selection can be achieved using Ctrl+left click. A single node can be selected using left click and can thereafter be removed in the same manner as above.
3. After inserting seeds on the current seismic inline, *move* the inline to a new location. For example, set Step to 10 and move inline in any direction.
 4. Proceed to *insert seeds* on new inline.
 5. After interpretation, the new fault can be saved either in the toolbar or in the tree.
 6. To save the *FaultStickSet*:
 - Right-click on the fault.
 - Select either “*Save*” or “*Save as...*” The latter enables you to specify a name and *Replace in tree*.

Faults can be interpreted in the seismic data from offsets in continuous amplitudinal reflectors. The offset will often vary between lower and upper reflectors, and can constrain the timing and re-activation periods of each fault.


Figure 2: Visible offsets of seismic reflectors either side of a normal fault (Crossline 2300, Ship Shoal 3D cube).



At the start of each new session the user will need to load the Dip Steered Median Filter for each cube, along with re-setting the horizon tracking settings. To load the attribute, click *Analysis* at the top left of the screen and select *Attributes*. Next select the *Open attribute set* icon and choose the attribute to be loaded. Finally, press *Ok* to continue. To load a horizon, right click *Horizon* and select *Add*. Choose the horizon in progress (i.e. *Top Salt Positive*), and press *Ok*. Next, right click the loaded horizon in the tree and select *Tracking > Start tracking*. A window will appear asking if you wish to specify the tracker settings, select *Yes*. An error window will appear asking you to “*Please*

select the seismic data to track on”, select *Ok*. Repeat the steps from Step 6, and select *Dismiss* to continue.

Step 8: Auto-track (pp. 65-67)

Once a horizon has been successfully tracked you will need to create a back-up. Right click the horizon in the tree and select “*Save As*”. A back-up is required as once a horizon has been produced in 3D you will be unable to go back and edit sections. To create a 3D horizon, select “*Auto-track*” .

Step 9: Attribute Analysis (pp. 96-98)

Attributes will be applied to both the tracked horizons and a selected Z-slice from each seismic cube. The Z-slices from each cube were selected on the basis that they illustrate seismic clarity, and intersect salt diapirism.

The attributes to be applied include the following, and can be calculate by:

➤ Dip (Azimuth)

1. Open the *Attribute Set 3D* window and select *Dip* for both dropdown menus.
2. Select *Steering_Background_Median_550* as the Steering Data and select the Output as *Azimuth*.
3. Name the attribute as *Dip_Background_AzimuthI* and select *Add as new*.

➤ Dip (Polar Dip)

1. Open the *Attribute Set 3D* window and select *Dip* for both dropdown menus.

2. Select *Steering_Background_Median_550* as the Steering Data and select the Output as *Polar Dip*.
 3. Name the attribute as *Dip_Background_PolarDip* and select *Add as new*.
- Minimum Curvature (Background Seismic Steering)
1. Open the *Attribute Set 3D* window and select *Dip* in the first dropdown menu, followed by *Curvature*.
 2. Select *Minimum Curvature* as the Output and select *Steering_Background_Median_550* as the Steering Data.
 3. Leave all other options as default and name the attribute *Minimum curvature_Background*.
- Maximum Curvature (Background Seismic Steering)
1. Open the *Attribute Set 3D* window and select *Dip* in the first dropdown menu, followed by *Curvature*.
 2. Select *Maximum Curvature* as the Output and select *Steering_Background_Median_550* as the Steering Data.
 3. Leave all other options as default and name the attribute *Maximum curvature_Background*.
- Full-steered Similarity (Detailed Seismic Steering)
1. Open the *Attribute Set 3D* window and select *Basic* in the first dropdown menu, followed by *Similarity*.
 2. Select *Dip_Steered_Median_Filter* as the Input Data and input -28, 28 as the Time gate (ms).
 3. In the Extension drop down menu select *Mirror 90* degrees and ensure Trace positions is *inl:0/crl:1 & inl:0/crl:-1* (default).

4. Choose Full in the Steering drop down menu and select *Steering_Detailed_BG111_MF113* as the Steering.
 5. Select Min as the Output statistic and name the attribute *Full-steered_Detailed_Similarity*.
- Full-steered Similarity (Background Seismic Steering)
1. Open the *Attribute Set 3D* window and select *Basic* in the first dropdown menu, followed by *Similarity*.
 2. Select *Dip_Steered_Median_Filter* as the Input Data and input -28, 28 as the Time gate (ms).
 3. In the Extension drop down menu select *Mirror 90* degrees and ensure Trace positions is *inl:0/crl:1 & inl:0/crl:-1* (default).
 4. Choose Full in the Steering drop down menu and select *Steering_Background_Median_550* as the Steering.
 5. Select Min as the Output statistic and name the attribute *Full-steered_Background_Similarity*.
- Non-steered Similarity
1. Open the *Attribute Set 3D* window by selecting *Analysis>Attributes*.
 2. In the first drop down menu select *All* followed by *Similarity* in its adjacent counterpart.
 3. Select *Dip_Steered_Median_Filter* as the Input Data and leave the default Time gate (ms) as -28, 28.
 4. Select *Mirror 90 degrees* as the Extension and ensure Trace positions is *inl:0/crl:1 & inl:0/crl:-1* (default).
 5. Select *None* as the Steering and choose *Min* as the Output Statistic.

6. Name the attribute *Non-steered_Similarity* and *Add as new*.

➤ Ridge Enhancement Filter (REF)

1. Open the *Attribute Set 3D* window and open the default set called: *Ridge enhancement filter*.
2. Select *Ship_Shoal_Area_1* or *NW_GC* as the seismics and *Dip_Steered_Median_Filter* as the steering cube.
3. Apply the Ridge enhancement filter to the seismic data in batch: *Processing - Create seismic output*, or on-the-fly: right-click on the element in the tree (e.g. part of a time-slice).

➤ Ridge Enhancement Filter

The filter compares in the time-slice domain three neighboring similarity values in six different directions and outputs the largest ridge value. The ridge in each direction is the: $\text{sum}(\text{values on either side}) / 2 - \text{center value}$. In most evaluation points there are no ridges and the values thus tend to be small but when you cross a fault there will be a large ridge perpendicular to the fault direction. The filter outputs the largest value i.e. the ridge corresponding to the perpendicular direction.

➤ Similarity

This attribute returns a value indication how much two or more trace segments look alike. Structurally, the attribute is useful in identifying faults and salt edges.

➤ Dip

A post-stack attribute that computes, for each trace, the best fit plane (3D) or line (2D) between its immediate neighbour traces on a horizon and outputs the magnitude of dip

(gradient) of said plane or line measured in degrees. This can be used to create a pseudo paleogeologic map on a horizon slice (Chopra and Marfurt 2007b).

➤ Azimuth

A post-stack attribute that computes, for each trace, the best fit plane (3D) between its immediate neighbour traces on a horizon and outputs the direction of maximum slope (dip direction) measured in degrees, clockwise from north (Chopra and Marfurt 2007b).

➤ Curvature

A group of post-stack attributes that are computed from the curvature of a specified horizon. These attributes include: magnitude or direction of maximum curvature, magnitude or direction of minimum curvature, magnitude of curvature along the horizon's azimuth (dip) direction, magnitude of curvature along the horizon's strike direction, magnitude of curvature of a contour line along a horizon (Chopra and Marfurt 2007b).

Comparison of these attributes on individual time slices will aim to identify sub-seismic amplitudinal features that represent fractures within the salt.